Check for updates

# BRD4 orchestrates genome folding to promote neural crest differentiation

Ricardo Linares-Saldana[1,2,3,13], Wonho Kim[1,2,3,13], Nikhita A. Bolar[1,2,3,13], Haoyue Zhang[4,5], Bailey A. Koch-Bojalad[1,2,3], Sora Yoon[1,3,6,7], Parisha P. Shah[1,2,3], Ashley Karnay[1,2,3], Daniel S. Park[1,3,6], Jennifer M. Luppino[1,3,6], Son C. Nguyen[1,3,6], Arun Padmanabhan[8,9], Cheryl L. Smith[1,2,3], Andrey Poleshko[1,2,3], Qiaohong Wang[1,2,3], Li Li[1,2,3], Deepak Srivastava[8,10], Golnaz Vahedi[1,3,6,7,11], Gwang Hyeon Eom[1,2,3,12], Gerd A. Blobel[1,3,5], Eric F. Joyce[1,3,6] and Rajan Jain[1,2,3]✉

**Higher-order chromatin structure regulates gene expression, and mutations in proteins mediating genome folding underlie developmental disorders known as cohesinopathies. However, the relationship between three-dimensional genome organization and embryonic development remains unclear. Here we define a role for bromodomain-containing protein 4 (BRD4) in genome folding, and leverage it to understand the importance of genome folding in neural crest progenitor differentiation. *Brd4* deletion in neural crest results in cohesinopathy-like phenotypes. BRD4 interacts with NIPBL, a cohesin agonist, and BRD4 depletion or loss of the BRD4–NIPBL interaction reduces NIPBL occupancy, suggesting that BRD4 stabilizes NIPBL on chromatin. Chromatin interaction mapping and imaging experiments demonstrate that BRD4 depletion results in compromised genome folding and loop extrusion. Finally, mutation of individual BRD4 amino acids that mediate an interaction with NIPBL impedes neural crest differentiation into smooth muscle. Remarkably, loss of WAPL, a cohesin antagonist, rescues attenuated smooth muscle differentiation resulting from BRD4 loss. Collectively, our data reveal that BRD4 choreographs genome folding and illustrates the relevance of balancing cohesin activity for progenitor differentiation.**

Organogenesis requires coordinated progressive lineage restriction and differentiation of progenitor cells into specific cell types. The neural crest is a population of cells critical for the development of several ectodermal and mesodermal tissues[1]. These cells delaminate from the neural tube and differentiate into a variety of specialized cells and tissues, including melanocytes, craniofacial bones and cartilage, and enteric nerves in the intestinal tract[2]. A subset of neural crest cells directs septation of the cardiac outflow tract and contributes to smooth muscle surrounding the aorta and pulmonary artery[3]. Impaired neural crest differentiation is implicated in the etiology of neurocristopathies, which often result in outflow tract morphogenesis defects, cleft palate and craniofacial abnormalities[4]. Thus, determination of the gene regulatory networks and molecular determinants underlying neural crest differentiation will inform our understanding of neurocristopathies and related diseases.

Emerging evidence links gene regulation to higher-order chromatin structure[5], suggesting a role for genome organization in development and tissue homeostasis. Recent studies have identified self-interacting areas of the genome that are important for gene expression. These domains are often composed of a nested series of discrete, and probably dynamic, chromatin interactions[6].

The physiological relevance of genome folding is of intense interest, as are the roles of specific genome organization factors in disease. The multisubunit cohesin ring complex has been shown to be a critical regulator of genome folding[7]. Loss of core cohesin complex subunits results in a loss of loop domains in population-based genomic studies[8,9]. Of particular interest, human mutations in the cohesin complex have been linked to leukemias and a group of diseases collectively termed cohesinopathies, which include Cornelia de Lange syndrome (CdLS) and related syndromes[10,11]. Multiple organ systems are often affected and syndromes share overlapping phenotypes. CdLS patients present with craniofacial abnormalities, including cleft lip and dental defects, intellectual disability and delayed ossification of various bones. Approximately one-third of patients also present with congenital heart disease[12]. Despite the rich human genetic data underlying cohesinopathies, the mechanistic relationship between cohesin function and pathogenesis remains unclear.

CdLS is frequently associated with heterozygous loss-of-function mutations in *NIPBL*, which encodes a positive effector of cohesin that facilitates loading of the cohesin on to chromatin[10,13,14]. In vitro reconstitution assays show that NIPBL enables cohesin to extrude loops of chromatin[15,16]. Accordingly, genetic loss of *Nipbl* in

mice results in a loss of topologically associating domains (TADs) and chromatin loops[17], and recapitulates phenotypes observed in cohesinopathies and CdLS[18]. It is interesting that patients with mutations in BRD4 can present with cohesinopathy features, particularly CdLS[19,20]. BRD4 is a member of the bromodomain and extraterminal domain (BET) protein family, characterized by tandem bromodomains that recognize acetylated lysine residues on histone and nonhistone proteins[21]. BRD4 is one of only a few non-core cohesin proteins that have been found to be mutated in CdLS. Although BRD4 and NIPBL interact[20,22], the functional nature of this relationship remains elusive, particularly if, and how, BRD4 modulates NIPBL and/or cohesin function and how this interaction directs tissue development.

BRD4 has a well-established role in recruiting transcriptional machinery on binding to acetylated histones to mediate transcriptional pause release[23]. In the present study, we reveal a role for BRD4 in mediating genome folding by stabilizing NIPBL on chromatin and thereby promoting neural crest progenitor differentiation. Loss of *Brd4* in neural crest cells in vivo results in phenotypes similar to cohesinopathies. Mechanistically, acute degradation of BRD4 results in diminished NIPBL chromatin occupancy and loss of normal genome folding, as assessed by high-throughput chromosome conformation capture (Hi-C). Oligopaints-based DNA FISH (Oligopaint FISH[24]) studies in cells acutely depleted of BRD4 or expressing BRD4 point mutants unable to bind NIPBL further demonstrate the importance of the BRD4–NIPBL complex in proper genome folding. Moreover, the role of BRD4 in genome folding is separate from its role in promoting transcription. Finally, a combination of in vivo and in vitro experiments demonstrates that BRD4 is required for neural crest differentiation into smooth muscle via an interaction with NIPBL. Remarkably, smooth muscle differentiation defects resulting from loss of BRD4 can be rescued by depletion of WAPL, a negative regulator of cohesin[25–28], demonstrating the functional relevance of BRD4 regulation of cohesin function. Taken together, by deciphering BRD4's role in maintaining genome topology, we establish the physiological relevance of balancing cohesin activity on cell fate determination.

## Results

**Brd4 loss in neural crest resembles cohesinopathies.** We crossed mice harboring loxP sites flanking exon 3 (canonical ATG) of *Brd4* (refs. [29,30]) with mice expressing Cre recombinase under the control of a *Wnt1* enhancer active in pre-migratory neural crest cells and neural crest immediately after their delamination from the neural tube[31]. We confirmed efficient, tissue-specific deletion of *Brd4* (Fig. 1a). We were unable to recover any mutant (*Brd4f/f*,*Wnt1*Cre+) embryos after postnatal day 1, indicating that BRD4 is essential in neural crest cells and required for development and mouse viability (Supplementary Table 1). BRD4-mutant late gestation embryos exhibited skeletal dysplasia coupled with several highly penetrant craniofacial defects including loss of forehead contouring, microcephaly, micrognathia and loss of neural-crest-derived middle-ear bones (Fig. 1b and Supplementary Table 1). In addition, all mutants demonstrated a cleft palate, which probably accounts for the observed perinatal lethality (Fig. 1c). Abnormal tooth formation was also observed (Fig. 1c, right). Despite loss of BRD4, neural crest derivatives were still able to populate the developing craniofacial structures as evidenced by lineage-tracing studies (Fig. 1d and Extended Data Fig. 1a).

Consistent with the role of the neural crest in outflow tract development, most late gestation *Brd4f/f*,*Wnt1*Cre+ embryos analyzed showed ventricular septal defects (VSDs) compared with zero littermate controls (Fig. 1e and Supplementary Table 1). Approximately half of late gestation embryos demonstrated more complex heart defects, including persistent truncus arteriosus, double-outlet right ventricle (DORV) and abnormal aortic arch artery

patterning, consistent with a defect in the cardiac neural crest[3] (Fig. 1e, Extended Data Fig. 1b and Supplementary Table 1). Given the craniofacial and cardiac abnormalities observed, we assessed proliferation in neural-crest-derived mesenchyme. We found a significant reduction in the percentage of phospho-histone H3-positive cells at embryonic day 11.5 (E11.5) in *Brd4f/f*,*Wnt1*Cre+,*R26mt-mg/+* embryos compared with *Brd4f/+*,*Wnt1*Cre+,*R26mt-mg/+* embryos consistent with the known role of BRD4 in cell proliferation (Extended Data Fig. 1c).

Collectively, these data establish that neural-crest-specific *Brd4* deletion results in a range of craniofacial, skeletal and cardiac defects, coupled with perinatal lethality. Loss of *Nipbl* or its related factor *Mau2* during embryogenesis results in a similar phenotype to those observed in the *Brd4f/f*,*Wnt1*Cre+ embryos[18,32] (Supplementary Table 1). Heterozygous global loss of *Nipbl*, including on a sensitized genetic background, results in VSDs and outflow tract defects[32]. Notably, expression of *Nipbl* and *Smc1a*, a subunit of the cohesin ring, were not affected by loss of *Brd4* in the neural-crest-derived secondary palate of *Brd4f/f*,*Wnt1*Cre+ embryos (Extended Data Fig. 1d). Given these phenotypes within the context of recent BRD4–CdLS human genetic studies mentioned above, we examined the interaction between BRD4 and NIPBL, and tested the hypothesis that loss of BRD4 results in aberrant NIPBL and/or cohesin function.

**A hydrophobic cleft in BRD4 ET domain mediates NIPBL interaction.** Reciprocal co-immunoprecipitation assays confirmed the known interaction between BRD4 and NIPBL[20,22] in murine embryonic stem cells (mESCs) and HEK293T cells (Fig. 2a). These results are consistent with previous studies in a cell-free system[22], as systematic analysis using human BRD4 (hBRD4) fragments (Fig. 2b) indicated that the extraterminal (ET) domain was sufficient to interact with NIPBL (Fig. 2c). Relevant to our mouse genetic studies, we immunoprecipitated endogenous BRD4 from neural crest progenitor cells[33] and observed co-precipitation of endogenous NIPBL (Extended Data Fig. 1e). Addition of a small-molecule degrader of BET proteins (MZ3 (ref. [34])) resulted in a reduction in the amount of BRD4 detected. Specificity of the interaction was further validated by reduction of the immunoprecipitation window to 30 min (Extended Data Fig. 1f). RAD21 and SMC1a, both cohesin ring subunits, and MAU2, which heterodimerizes with NIPBL[35], also co-immunoprecipitated with BRD4, although the band intensity of each protein was relatively weaker compared with NIPBL (Extended Data Fig. 1g,h).

Nuclear magnetic resonance spectroscopy studies have revealed the structure of the BRD4 ET domain[36] (Fig. 2d). To identify residues critical for NIPBL interaction, we generated a series of point mutations within a hydrophobic pocket of the ET domain that has been shown to be critical for interaction with proteins such as NSD3 (refs. [36,37]). We expressed either FLAG-tagged wild-type hBRD4 or full-length hBRD4 harboring various mutations in the ET domain. Deletion of the ET domain (dET) or introduction of point mutations (L630W, V634W, I654Q, F656W and E653R/D655R) into the hydrophobic pocket resulted in a reduction or loss of interaction with NIPBL (Fig. 2e). An ET domain point mutation (R669H) outside the hydrophobic pocket did not disrupt NIPBL binding (Fig. 2e). We found a similar trend with MAU2 (Extended Data Fig. 1i), consistent with a report indicating that MAU2 chromatin binding depends on NIPBL[35]. In addition, BRD4–L630W, –I654Q, –F656W and –E653R/D655R also eliminated the known interaction with NSD3 (ref. [37]), whereas BRD4–V634W did not perturb the NSD3 interaction to the same degree. All BRD4 mutants retained the ability to interact with histone H4 acetylated on lysines 5, 8, 12 and 16, known to be strongly bound by BRD4 (ref. [38]), suggesting that loss of NIPBL interaction was not a result of abrogated chromatin binding. Studies have identified peptide sequences from BRD4-interacting
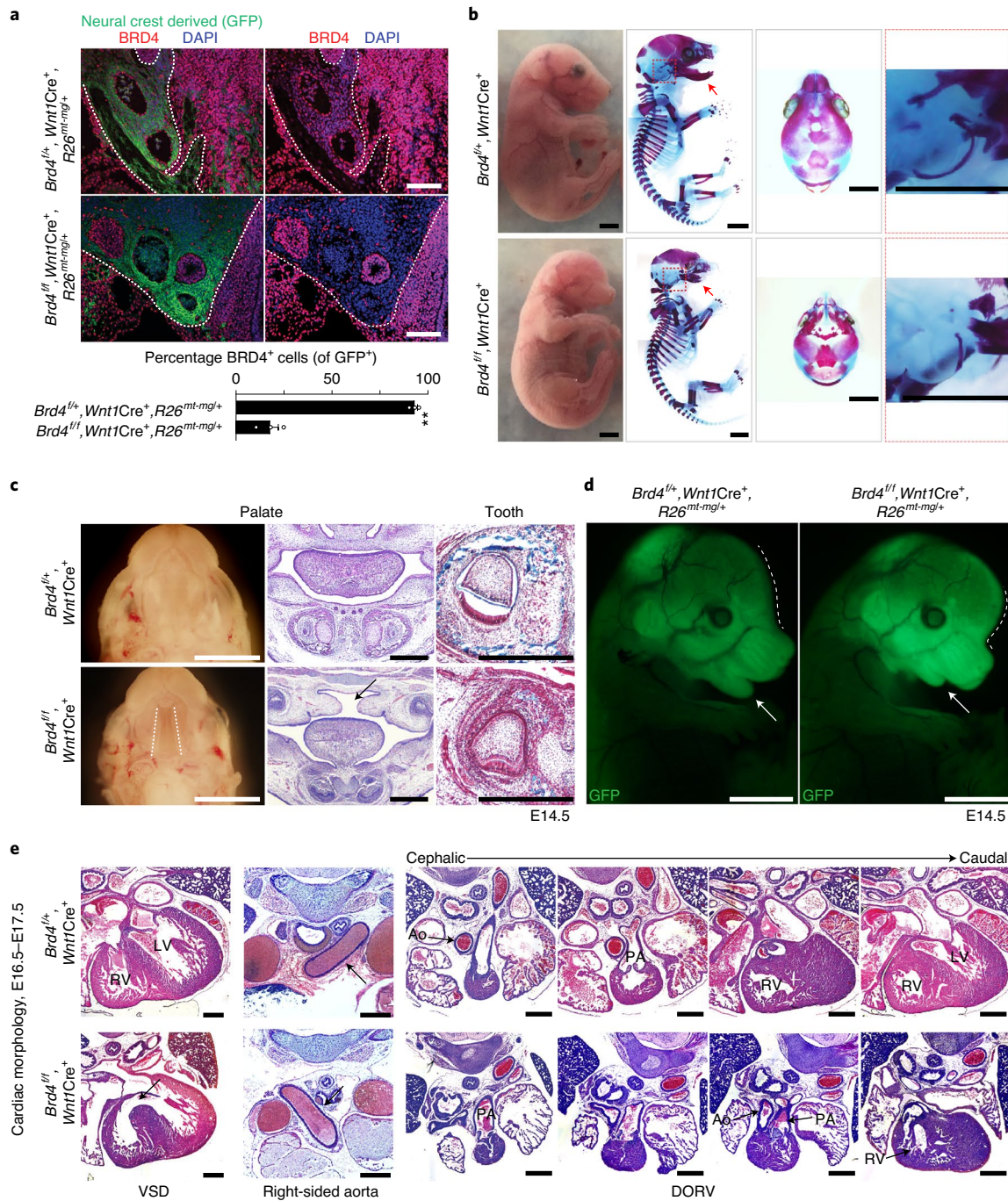
**Fig. 1 | Loss of Brd4 in neural crest cells results in cohesinopathy features. a**, Cross-section through aortic arch arteries of E11.5 *Brd4[f/f],Wnt1*Cre+,*R26[mt-mg/+]* and *Brd4[f/+],Wnt1*Cre+,*R26[mt-mg/+]* embryos stained with GFP (green, neural crest derivatives) and BRD4 (red). **P < 0.01, Student's *t*-test. Scale bars, 100 µm. All error bars denote the mean + s.e.m. **b**, BF (left) and skeletal prep images from E17.5 embryos. Sagittal view of the skeletal staining (left, composite image of multiple individual images) and axial view of the cranium (middle). The red arrow points to the mandible and the cochlear bones are magnified in the right panel (red box). Scale bars, 250 mm. **c**, Images of the secondary palate (whole mount and histology) and teeth in E14.5 embryos. The white dotted lines highlight the cleft palate in a mutant embryo. Adjacent to whole-mount images are H&E-stained coronal sections through the palate, and the arrow points to the cleft palate in a *Brd4[f/f],Wnt1*Cre+ embryo. On the right is a trichrome-stained coronal section through developing teeth, indicating reduction of collagen in a *Brd4[f/f],Wnt1*Cre+ embryo. Scale bars, 250 mm. **d**, Epifluorescence images of neural crest derivatives (GFP) in face of *Brd4[f/f],Wnt1*Cre+, *R26[mt-mg/+]* and *Brd4[f/+],Wnt1*Cre+,*R26[mt-mg/+]* embryos. The dotted line shows the altered curvature of the face in a mutant embryo and the arrow points to a hypoplastic mandible in the mutant. Scale bars, 250 mm. **e**, Cross-section histology of E16.5–E17.5 embryos showing examples of cardiac abnormalities in *Brd4[f/f],Wnt1*Cre+ embryos, specifically, VSD (left), right-sided aorta (R aorta, middle, arrow points to aortic arch; note that the aorta is coursing to the right in the mutant), DORV, aorta (Ao), pulmonary artery (PA), right ventricle (RV) and left ventricle (LV). Scale bars, 500 µm.
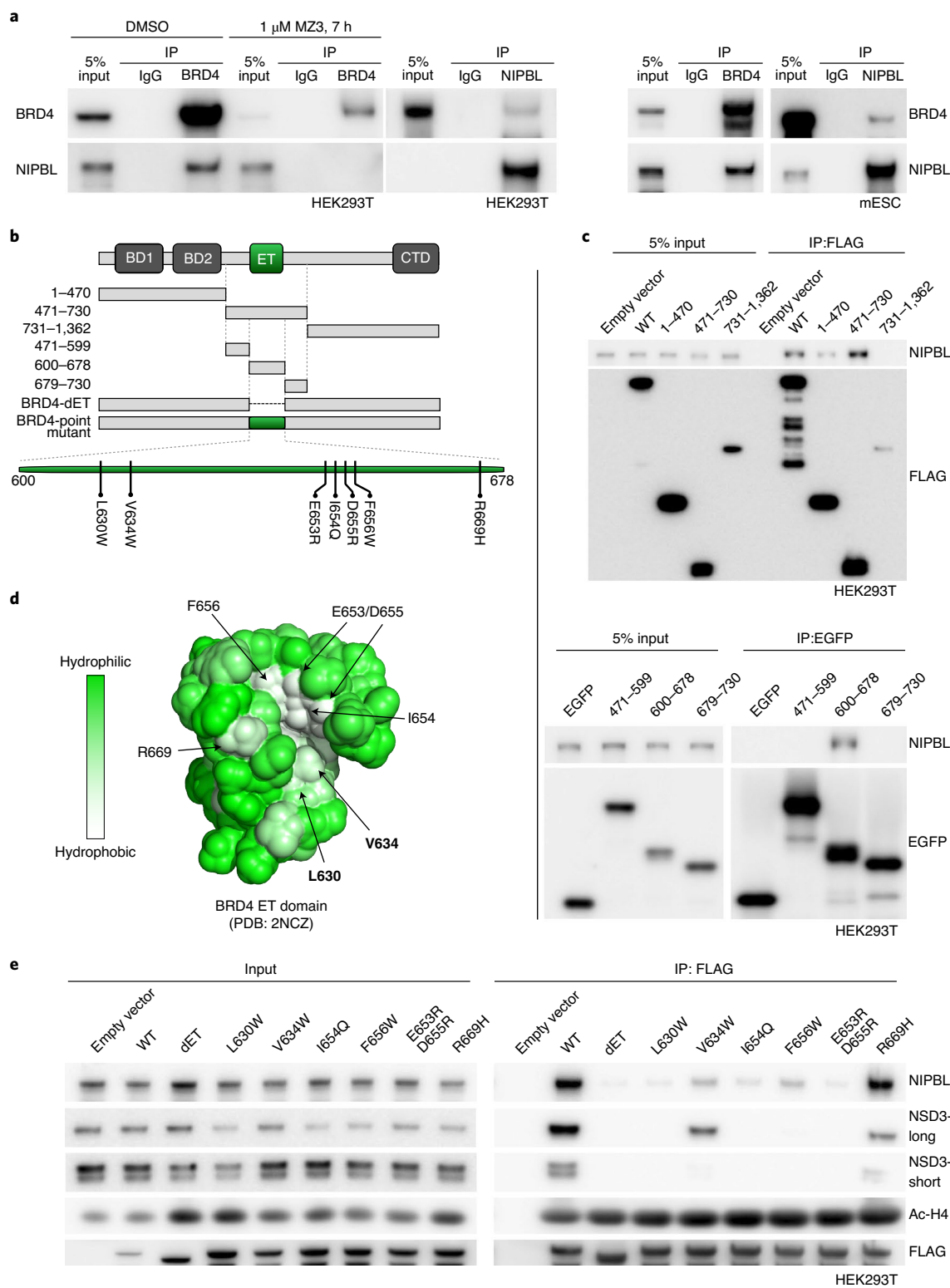
**Fig. 2 | BRD4 ET domain mediates a physical interaction with NIPBL. a**, Immunoprecipitation of endogenous BRD4 or NIPBL from HEK293T cells (left) or mESCs (right), and western blots probed with BRD4 or NIPBL antibody. BRD4 was immunoprecipitated in HEK293T cells treated with DMSO or 1 μM MZ3 for 7 h. **b**, Domain structure of BRD4 (long isoform) with schema of fragments evaluated and point mutations introduced highlighted. **c**, FLAG- or enhanced GFP (EGFP)-tagged BRD4 peptides were expressed and immunoprecipitated in HEK293T cells. Western blots were probed with NIPBL, FLAG (top) and EGFP (bottom) antibodies. **d**, Structure of ET domain of BRD4 highlighting the hydrophobic cleft[36]. Amino acids mutated in subsequent experiments are emboldened. **e**, Indicated FLAG-tagged versions of BRD4 were expressed and immunoprecipitated in HEK293T cells. Western blots were probed with the indicated antibodies. NSD3-long and -short indicate long and short isoforms of NSD3, respectively. Ac-H4 indicates acetylated histone H4.

proteins that may bind the ET domain (Extended Data Fig. 1j)[36,39]. Alignment of these sequences revealed a consensus motif of Φ-K/R-Φ-X-K/R (Φ, hydrophobic amino acid; X, any amino acid). A sequence in the N terminus of NIPBL aligns with the consensus sequence, and it is predicted to have an α-helical structure similar to the BRD4-interacting domain in JMJD6 (Extended Data Fig. 1j)[40]. Collectively, these biochemical experiments identify the specific residues within the hydrophobic cleft of the BRD4 ET domain that mediate this interaction.

**BRD4 stabilizes NIPBL binding on chromatin.** Consistent with our interaction studies, previous reports have shown that BRD4 and NIPBL both co-occupy regulatory elements[41,42]. Analysis of publicly available mESC chromatin immunoprecipitation (ChIP)–sequencing datasets (GSM937540–BRD4, GSM560350–NIPBL) revealed that ~66% of peaks were co-occupied by BRD4 and NIPBL (21,327 shared sites, 34,794 total BRD4 sites and 34,942 total NIPBL sites; Extended Data Fig. 2a and Supplementary Table 2). Therefore, we sought to assess whether BRD4 is necessary for NIPBL occupancy on chromatin. We generated mESCs in which a degron epitope tag (dTAG) was introduced immediately after the conserved endogenous start codon of *Brd4* on both alleles[43] (hereafter referred to as dTAG–BRD4 mESCs; Fig. 3a and Extended Data Fig. 2b,c). The dTAG insertion was confirmed by PCR amplification and Sanger sequencing (Extended Data Fig. 2b). Introduction of the epitope did not substantially alter the levels of chromatin-bound BRD4 in the dTAG–BRD4 mESCs compared with the parental mESC line (Extended Data Fig. 2c). Addition of a dTAG ligand (dTAG-13), renders the tagged BRD4 protein sensitive to proteasomal degradation, enabling depletion of BRD4 in an acute and efficient manner (dTAG-13-treated dTAG–BRD4 mESCs, hereafter 'degron'). All experiments, unless otherwise indicated, used naive mESCs, in which the short isoform of BRD4 is not expressed[44]. After optimizing isolation of chromatin fractionations (Extended Data Fig. 2d), we confirmed that chromatin-bound BRD4 was efficiently degraded in both a dTAG-13 dose- and time-dependent manner (Fig. 3b,c). In addition, OCT4 (also known as POU5F1) was expressed in dTAG–BRD4 mESCs treated with either dimethyl sulfoxide (DMSO) or dTAG-13 for 4.5 h (Extended Data Fig. 2e). Importantly, acute degradation of BRD4 for 4.5 h did not result in substantial changes in proliferation compared with DMSO-treated dTAG-BRD4 mESCs (Extended Data Fig. 2f). Taking this into account, and the estimated mESC doubling time of ~8–10 h[45], we proceeded with experiments using cells treated with dTAG-13 or DMSO for 4.5 h (unless otherwise noted).

We employed cleavage under target and release under nuclease (CUT&RUN) to map BRD4 and NIPBL occupancy in dTAG–BRD4 mESCs treated with DMSO or degron (*n* = 3 replicates; Supplementary Table 2). After confirming reproducibility, datasets were merged, scaled and read-depth normalized for intra-condition comparison as previously described[46] (see Methods; Supplementary Table 2). We detected enrichment of NIPBL and BRD4 at previously defined BRD4 and NIPBL peaks, as well as substantial co-occupancy between the factors in DMSO-treated cells (Fig. 3d,e and Extended Data Fig. 3a). In addition, BRD4 occupancy was dramatically reduced in the degron samples (Fig. 3d,e and Extended Data Fig. 3a). Strikingly, NIPBL occupancy was also decreased in the degron samples (Fig. 3d,e and Extended Data Fig. 3a,b). Furthermore, we also observed a moderate reduction in chromatin-bound NIPBL in cells treated with dTAG-13, dTAG^v-1, an alternative dTAG ligand[47] or MZ3 (Extended Data Fig. 3c). Similarly, we performed CUT&RUN to assess acetylation of lysine 27 on histone H3 (H3K27ac), a post-translational modification enriched at active regulatory regions[48]. We confirmed enrichment of H3K27ac in DMSO-treated cells at previously annotated H3K27ac peaks (GSM2588454) and observed no clear changes in the H3K27ac profile in the degron samples (Fig. 3d,e and Extended Data Fig. 3a), indicating that reduced NIPBL occupancy and other phenotypes described below that result from BRD4 depletion cannot be attributed to H3K27ac loss.

We next assessed whether the BRD4–NIPBL interaction was necessary to maintain NIPBL on chromatin by leveraging the aforementioned NIPBL-binding, defective BRD4 mutants (BRD4–dET, –L630W and –V634W). First, we established conditions in which the expression levels of exogenous wild-type or BRD4 mutants were comparable across conditions upon degradation of endogenous BRD4 (Extended Data Fig. 3d). Next, we performed ChIP–quantitative (q)PCR at two loci with substantial BRD4 and NIPBL occupancy (Fig. 3e,f). Loss of endogenous BRD4 resulted in a significant reduction in NIPBL occupancy, but unchanged H3K27ac enrichment (Fig. 3f and Extended Data Fig. 3e). Importantly, exogenous expression of full-length BRD4 normalized NIPBL occupancy, whereas expression of BRD4 ET deletion or point mutants reduced NIPBL occupancy at both loci (Fig. 3f). BRD4 enrichment was comparable at these sites in the cultures expressing exogenous BRD4 (Extended Data Fig. 3f). Together, these data support a model in which BRD4 stabilizes NIPBL on chromatin, probably through an interaction in the ET domain.

**BRD4 maintains genome folding by interacting with NIPBL.** Loss of *Nipbl* in postnatal hepatocytes results in a loss of chromatin loops and a weakening of TADs[17]. Given the decrease in NIPBL occupancy on acute BRD4 depletion, we assessed the impact of acute BRD4 loss on higher-order chromatin organization. We performed in situ Hi-C[49] in two biological replicates of DMSO and degron dTAG–BRD4 mESCs, each (Fig. 4a). After confirming the data quality and reproducibility, replicate reads were pooled, mapped, filtered for valid interactions, binned and normalized based on the Hi-C-Pro pipeline to generate normalized and balanced contact maps[50] (see Methods; Supplementary Table 2). In total, we sequenced ~1 billion paired-end reads per condition, which resulted in 291,168,696 and 245,410,300 contacts from the DMSO- and degron-treated cells, respectively, post-filtering.

Visual inspection of interaction matrices suggested a general weakening of interactions on acute BRD4 loss (Fig. 4a). To quantitatively assess changes genome wide, we identified focal areas of high interaction frequency between two distal regions of the genome, often referred to as chromatin loops[7,51,52]. We benchmarked loop-calling algorithms against a high-resolution mESC contact matrix[53] and arrived at an optimal set of parameters using cLoops[54] to identify chromatin loops that substantially overlapped with previously published SMC1a-anchored loops[55] (Extended Data Fig. 4a). Approximately half of the loops in DMSO-treated cells were associated with a BRD4 peak at one or both anchors (*n* = 3,860/7,517). Moreover, the strength of loops identified in DMSO cells significantly decreased on BRD4 depletion (Fig. 4b,c and Supplementary Table 3). We then stratified loops as either lost (sensitive to BRD4 loss and hence identified in DMSO but not in degron; hereafter 'BRD4 sensitive') or retained (resistant to BRD4 loss and identified in both conditions; hereafter 'BRD4 resistant'). The majority of loops in the DMSO dataset were BRD4 sensitive (*n* = 5,298/7,517 loops), and therefore not identified in the degron condition. There was a reduction in the contact frequency (normalized mean counts per bin) for BRD4-sensitive loops on BRD4 depletion (Fig. 4b) and aggregate analysis of this loop subset confirmed sensitivity to BRD4 depletion (Fig. 4c). Approximately 30% of loops identified in DMSO were BRD4 resistant (Fig. 4b,c, *n* = 2,219/7,517). Although BRD4-resistant loops lost strength on BRD4 depletion, as expected the change in strength was not as dramatic as for BRD4-sensitive loops. Our analyses also revealed newly formed loops in the degron condition, but there was a minimal increase in counts in the degron condition, especially in comparison to the change observed in
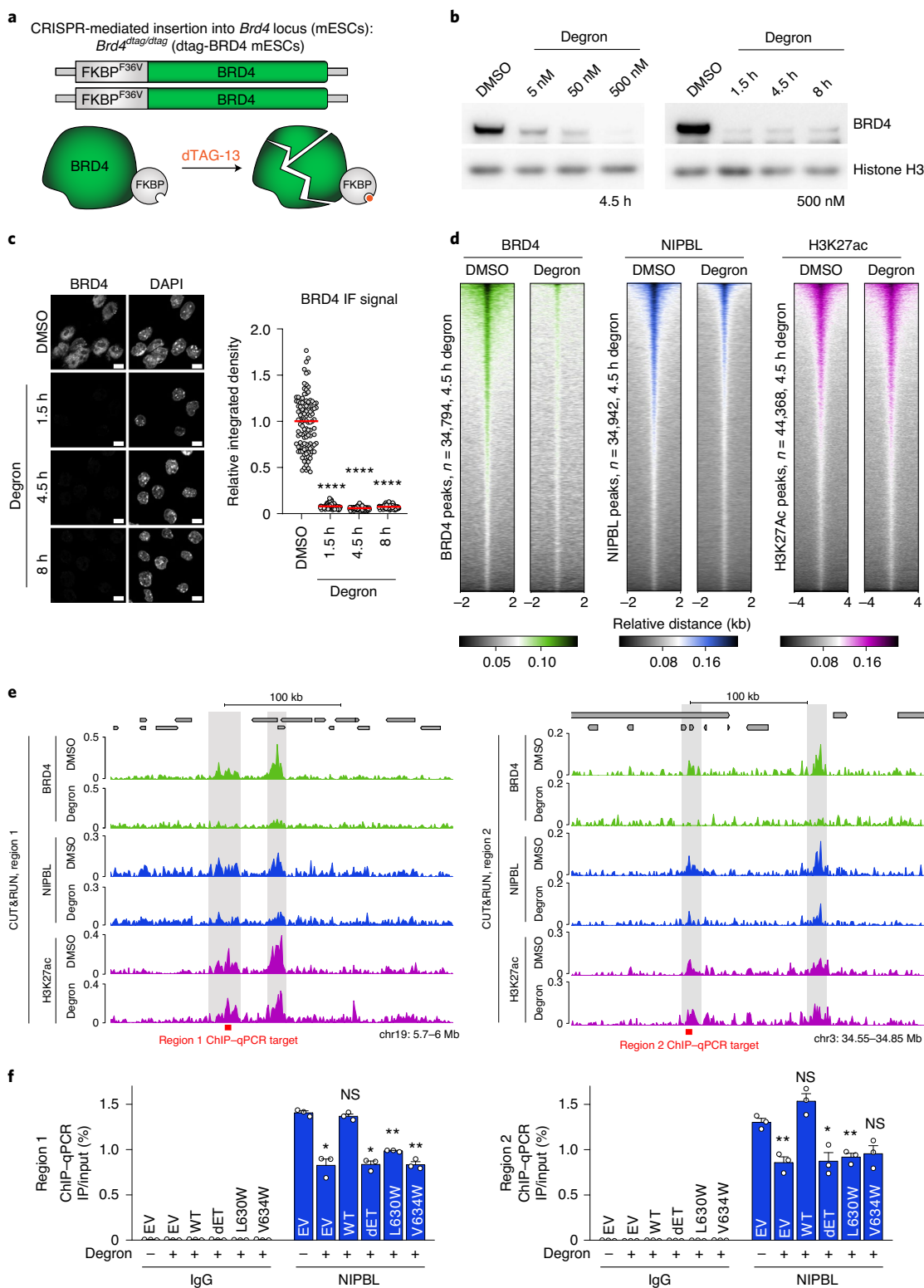
**Fig. 3 | Acute degradation of BRD4 reduces NIPBL occupancy on chromatin. a**, Schema of generating dTAG–BRD4 mESCs. **b**, Western blot of BRD4 and histone H3 on chromatin fractions from dTAG–BRD4 mESCs in various concentrations of dTAG-13 (left) or time (right). **c**, IF of BRD4 and DAPI from dTAG–BRD4 mESCs treated with 500 nM dTAG-13, and associated quantification of integrated BRD4 IF signal per cell (****$P \leq 0.0001$). Mean values are indicated by the red lines. Scale bar, 10 μm. **d**, Heatmap of BRD4 (green), NIPBL (blue) and H3K27ac (purple) occupancy (normalized counts) in the DMSO and degron (4.5 h) conditions at published peaks of each factor. **e**, CUT&RUN tracks of BRD4 (green), NIPBL (blue) and H3K27ac (purple) in the DMSO or degron (4.5 h) conditions at two different representative locations. ChIP–qPCR targets indicated in red. The genes are shown on top of the track in gray. **f**, ChIP–qPCR of NIPBL at regions indicated in **e** in dTAG–BRD4 mESCs in the DMSO or degron conditions. Indicated full-length BRD4 or BRD4 mutants that cannot bind NIPBL were simultaneously expressed. One-way analysis of variance (ANOVA), Dunnett's test was used to compare conditions to empty vector (EV) transfection with DMSO treatment. *$P < 0.05$, **$P < 0.01$. NS, not significant. Error bars denote the mean + s.e.m.
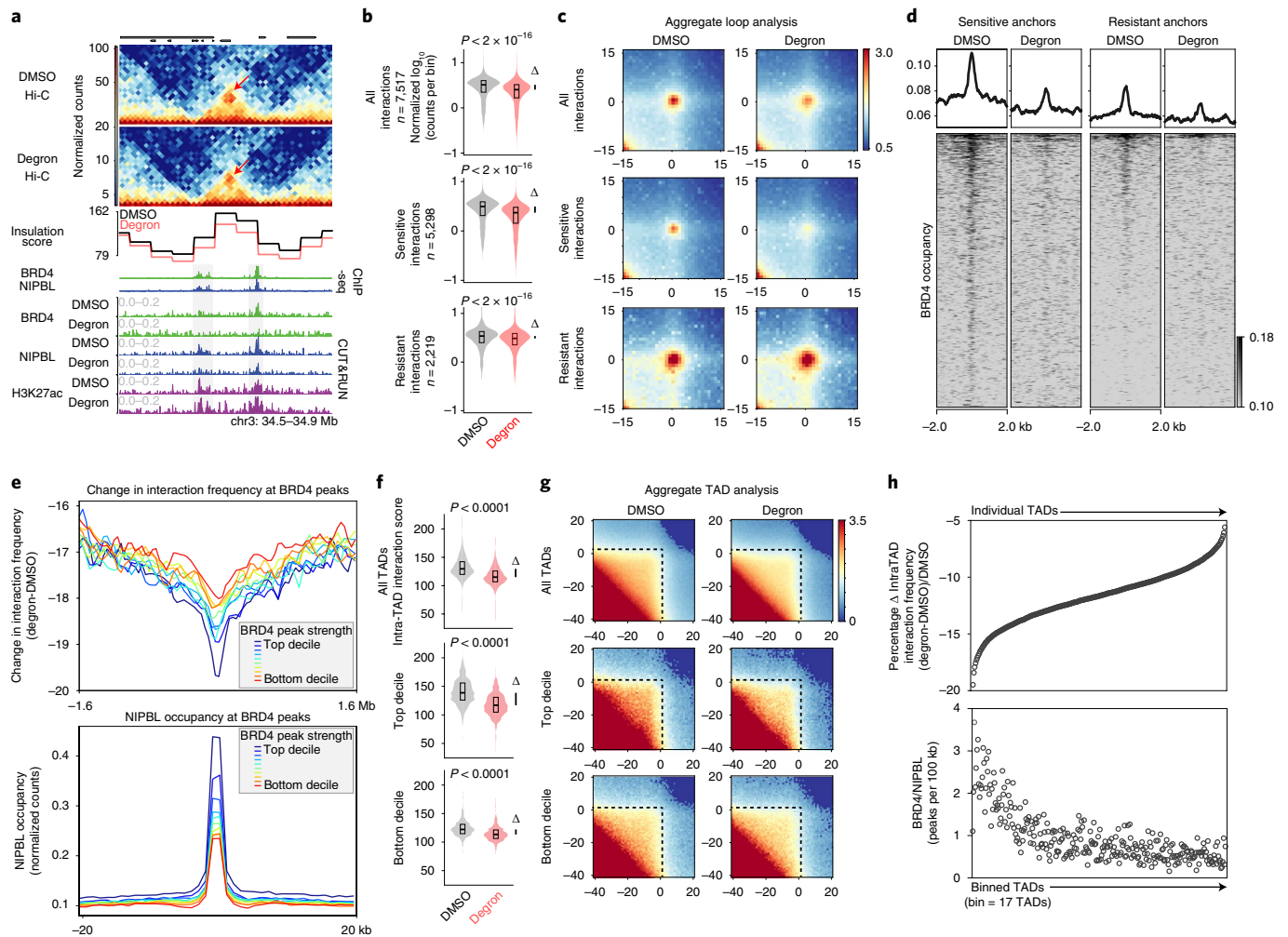
**Fig. 4 | BRD4 maintains genome folding. a**, Insulation score and representative Hi-C matrix view (10-kb resolution) in the DMSO and degron (4.5 h) conditions with occupancy of BRD4 (green), NIPBL (blue) and H3K27ac (purple) below. Occupancy from publicly available BRD4 and NIPBL ChIP–seq datasets in mESCs is also shown. Genes are shown above the Hi-C matrix in gray. The red arrow points to the corner peak which is weaker in the degron condition. **b,c**, Violin plots (**b**) of mean counts per bin in indicated subsets of chromatin loops and associated aggregate plot analysis (**c**). Student's *t*-test was used for comparison. **d**, BRD4 occupancy (normalized counts) at anchors of BRD4-sensitive and -resistant interactions in the DMSO or degron conditions. Note the enrichment of BRD4 at the anchors of BRD4-sensitive loops. **e**, Change in interaction frequency at BRD4 peaks (stratified into deciles of peak strength) on depletion of BRD4 (top). NIPBL occupancy (normalized counts) at stratified BRD4 peaks in the DMSO condition (bottom). **f,g**, Violin plots of interaction frequency (**f**) and associated aggregate plots (**g**) of different subsets of TADs in the DMSO and degron conditions. Two-tailed Student's *t*-test was used for comparison in **f**. Color bars in **c** and **g** refer to the enrichment score. **h**, Percentage change in intra-TAD interaction frequency on BRD4 loss of regions defined as TADs in the DMSO condition (ranked in descending change in frequency order, top). Number of BRD4/ NIPBL peaks (per 100 kb) per 17 consecutive TADs shown below (ordered based on descending change in interaction frequency). Bar under Δ in **b** and **f** indicates median-to-median difference. All boxes in violin plots indicate the median and interquartile range.

BRD4-sensitive loops (Extended Data Fig. 4b). Therefore, we focused subsequent analyses on BRD4-sensitive and BRD4-resistant regions/loops.

BRD4-sensitive loop anchors were enriched for BRD4 and NIPBL occupancy compared with BRD4-resistant loop anchors (Fig. 4d and Extended Data Fig. 4c). Furthermore, most BRD4-resistant loops were enriched for features consistent with structural loops, previously defined as loops containing CTCF and cohesin peaks at both anchors and H3K27ac peaks at no more than one anchor[56] (Extended Data Fig. 4d). In a reciprocal approach, we calculated genome-wide insulation scores in 40-kb bins in DMSO- and degron-treated cells, and calculated the change in interaction frequency around BRD4 and NIPBL peaks. The interaction frequency inversely correlates with the insulation score[57], and interaction frequency decreased around regions identified as BRD4 or

NIPBL peaks, as opposed to regions bound by other architectural proteins (Extended Data Fig. 4e). Visual inspection of the interaction matrices and the loop analyses suggests that some regions are more vulnerable to decreases in interaction frequency than others on BRD4 degradation, and the amount of BRD4 and NIPBL occupancy broadly correlated (Extended Data Fig. 3a). Therefore, we plotted change in interaction frequency based on stratification of BRD4 and NIPBL peak strength in DMSO-treated cells. Areas with the highest BRD4 peak strength showed the greatest decrease in interaction frequency, and these regions also displayed the greatest NIPBL occupancy. In contrast, areas with weaker BRD4 peaks demonstrated smaller changes in interaction frequency and lower NIPBL occupancy (Fig. 4e). A similar trend was also observed for changes in interaction frequency relative to NIPBL peak strength (Extended Data Fig. 4f).
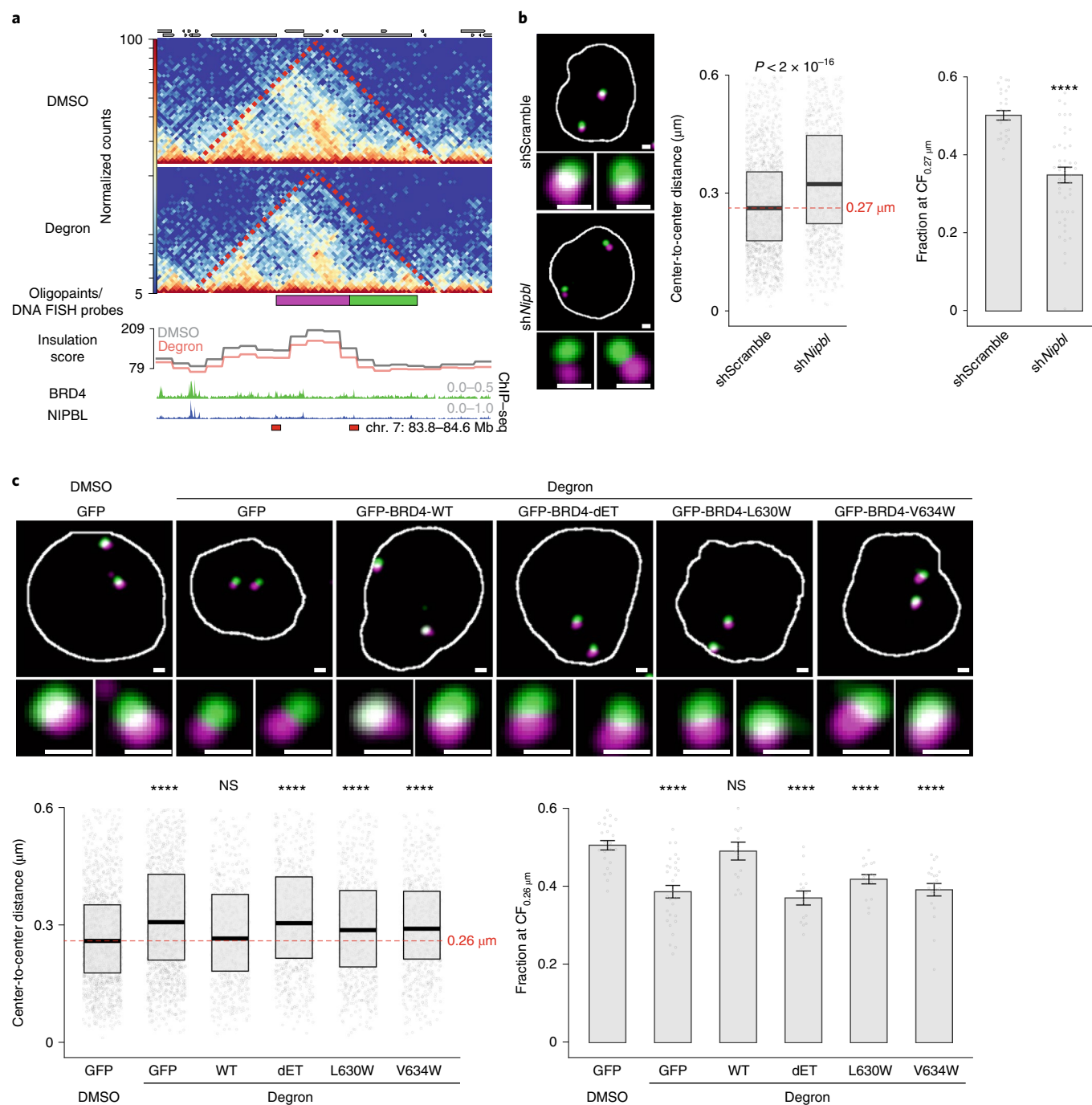
**Fig. 5 | A BRD4–NIPBL interaction is necessary for genome organization. a**, Hi-C matrix (10-kb resolution) of genomic region painted with Oligopaints (as indicated by the green and magenta bars below the matrix). Below the matrix is the insulation score and occupancy of BRD4 and NIPBL (ChIP–seq) in mESCs. The two red bars below the matrix indicate the targets for ChIP–qPCR (Extended Data Fig. 6g). Regions 1 and 2 in Extended Data Fig. 6g are indicated by left and right bars, respectively. **b**, Representative images of DNA FISH to regions indicated in **a** in dTAG–BRD4 mESCs expressed with shScramble or sh*Nipbl*. Adjacent to images are plots of center-to-center distance (*n* > 1,000, each condition, Welch's two-sample *t*-test) and a fraction of the signals in each field of view below the median contact frequency (0.27 μm, red dotted line) of center-to-center distance in the shScramble condition (****$P < 0.0001$, Wilcoxon's rank-sum test). **c**, Representative Images of DNA FISH of regions indicated in **a** in dTAG–BRD4 mESCs treated with DMSO or dTAG-13 for 4.5 h. Cells were also transfected with plasmids encoding indicated BRD4 fragment (or GFP control). Below the high-magnification images is the quantification of center-to-center distance (*n* > 700, each condition; all comparisons against GFP/DMSO; ****$P < 0.0001$, Wilcoxon's rank-sum test) and the fraction of the signals in each field of view at median contact frequency of center-to-center distance in GFP/DMSO conditions (all comparisons to GFP/DMSO; ****$P < 0.0001$, Wilcoxon's rank-sum test). NS, not significant. CF denotes contact frequency at 0.26 μm (red dotted line). For visualization purposes only, only probe center-to-center distances up to 0.6 μm are shown in the barplots in **b** and **c**. Scale bars, 1 μm. All error bars denote the mean ± s.e.m.; all boxes indicate the median and interquartile range. All images are maximum intensity projected. The nucleus boundary is marked by the white line.
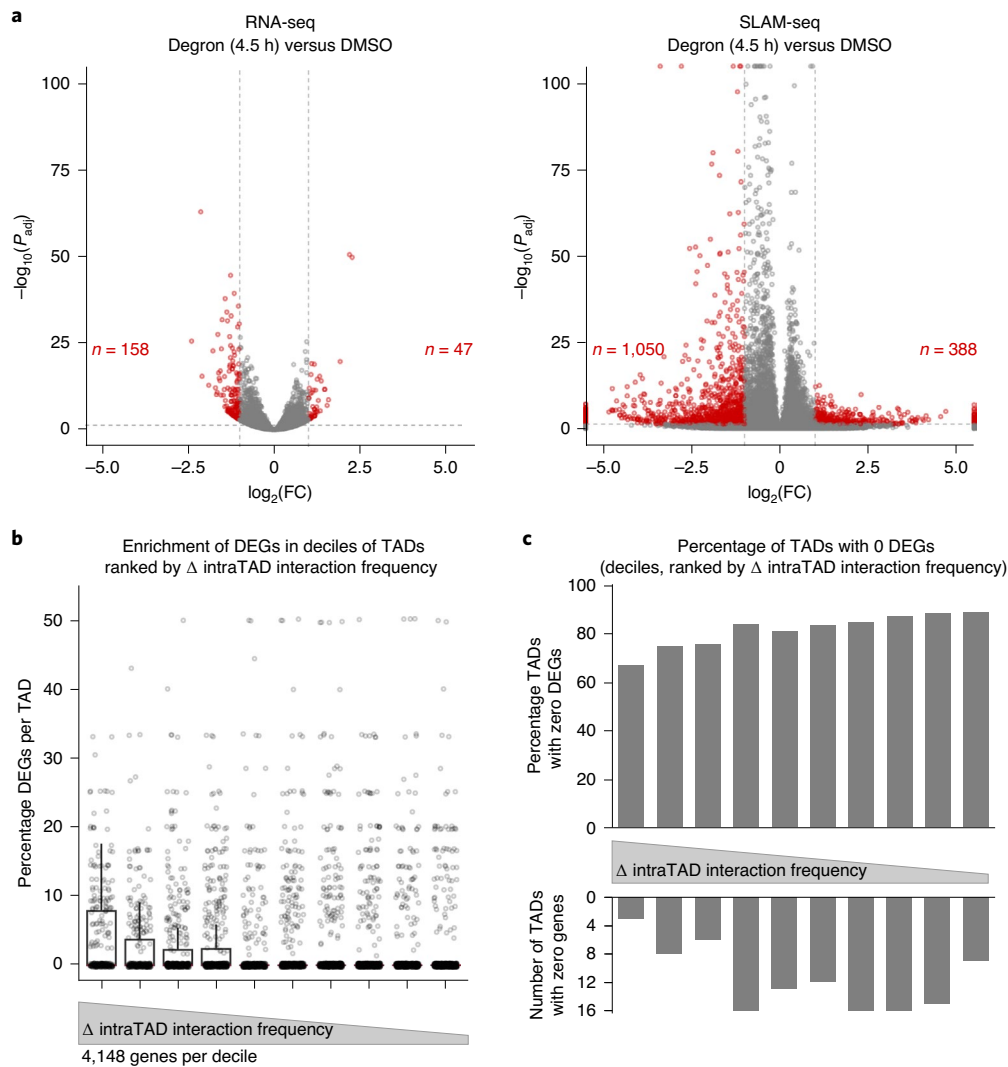
**Fig. 6 | Changes in transcription dynamics on BRD4 depletion. a**, Volcano plots plotting change in gene expression in the degron (4.5 h) versus DMSO conditions. On the left is RNA-seq whereas the right shows the increased sensitivity of SLAM-seq. The dotted lines indicate thresholds used to defined differential expression (FDR > 0.05, $\log_2(FC) > 1$). The number of upregulated or downregulated genes is indicated on the plots. **b**, The percentage of differentially expressed genes per TAD plotted and TADs broken into descending deciles of change in interaction frequency. Individual TADs are shown, as well as a superimposed box-and-whisker plot (median and interquartile range indicated by box). Only TADs with at least one gene are plotted. **c**, Percentage of TADs at each decile with zero differentially expressed genes (top) and number of TADs with zero genes (bottom).

In addition to changes in chromatin loops, visual inspection of the interaction matrix suggested a weakening of TADs[51] (Fig. 4a). We identified ~4,800 TADs in DMSO-treated dTAG–BRD4 mESCs, similar to previous reports (Jaccard index = 0.82 compared with Dixon et al.[51]; Extended Data Fig. 4g and Supplementary Table 3)[53]. TADs showed reduced interaction frequency/weakening on BRD4 depletion (Fig. 4f,g, top row). To extend this observation, we determined the percentage change in the mean interaction frequency for each TAD defined in the DMSO dataset on BRD4 depletion (Fig. 4h). This assessment confirmed that a subset of TADs was uniquely sensitive to BRD4 depletion (Fig. 4f,g; top and bottom deciles of TADs changing, respectively) and, similar to the loop analysis, BRD4-sensitive TADs were also enriched in BRD4/NIPBL peaks (Fig. 4h). Moreover, unlike intra-TAD interaction frequency, we found that insulation at boundaries between TADs did not vary substantially (DMSO and degron insulation score, Spearman's correlation = 0.97; Extended Data Fig. 4h). Finally, we did not detect substantial changes in compartmentalization (Extended Data Fig. 5).

Taken together, these data indicate that organization of a subset of loops and TADs are dependent on BRD4.

To validate the Hi-C findings, we designed Oligopaint FISH probes to three genomic regions that demonstrated a reduction in NIPBL occupancy and interaction frequency upon BRD4 depletion (Fig. 5a, Extended Data Fig. 6a,d,e and Supplementary Table 4). Our group has shown that TAD changes can be visualized using such an approach[58]. NIPBL depletion resulted in a significant increase in the center-to-center distance between FISH signals (Fig. 5a,b and Extended Data Fig. 6b), consistent with published reports[17,25,58]. BRD4 depletion also resulted in a significant increase in center-to-center distance between signals with minor changes in individual probe geometry (Fig. 5a,c and Extended Data Fig. 6c; representative replicate shown). We also observed increased center-to-center FISH probe distances at a different locus with the aforementioned characteristics (Extended Data Fig. 6d). A third locus with less BRD4 and NIPBL occupancy in DMSO samples than the other two loci (and at which we observed a smaller change in interaction frequency in our
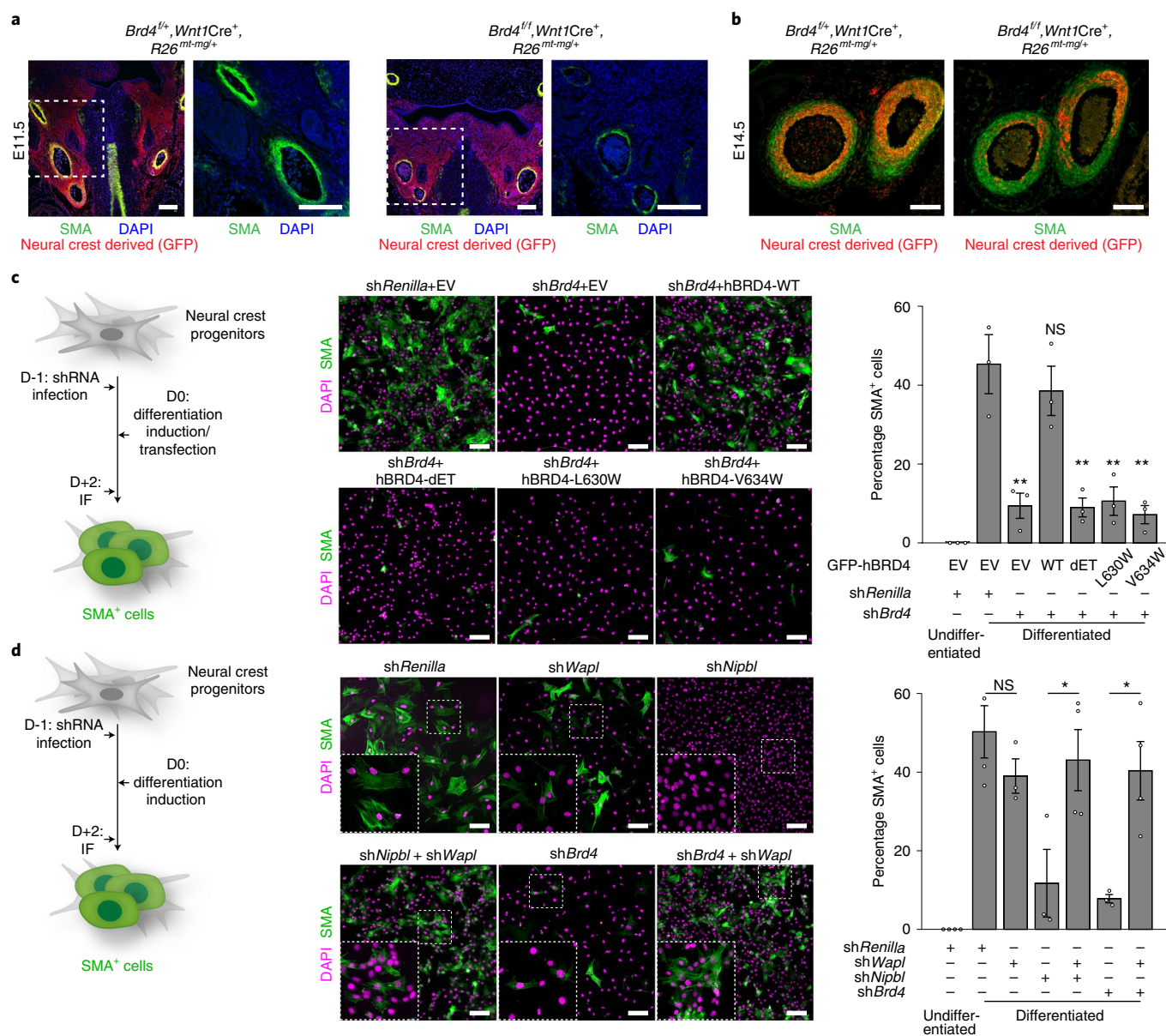
**Fig. 7 | A BRD4–NIPBL interaction promotes smooth muscle cell differentiation of neural crest cells. a,b,** Coronal section of E11.5 (**a**) and E14.5 (**b**) $Brd4^{f/+},Wnt1Cre^+,R26^{mt-mg/+}$ and $Brd4^{f/+},Wnt1Cre^+,R26^{mt-mg/+}$ aortic arch arteries stained with GFP (red, neural crest derivatives) and SMA (green). The area in the box is magnified in the middle panel of **a**. Scale bar, 100 µm. **c**, Differentiation of neural crest progenitor cells (O9-1 cells) on knockdown of endogenous $Brd4$ and exogenous expression of indicated human BRD4 mutants unable to bind NIPBL. Schema is on the left, representative images of SMA (green) and DAPI (magenta) are in the middle, and quantification of replicate experiments is tallied on the right. EV, empty vector. **\*\***$P < 0.01$, ANOVA followed by Dunnett's test. NS, not significant. Scale bar, 100 µm. All error bars denote the mean ± s.e.m. **d**, Differentiation of neural crest progenitor cells (O9-1 cells) on knockdown of indicated factors, individually or in combination. The schema is on the left, representative images of SMA (green) and DAPI (magenta) are in the middle, and insets display higher magnification images of the outlined area, with quantification of replicate experiments tallied on the right. *$P < 0.05$, ANOVA followed by Tukey's test. Scale bar, 100 µm. All error bars denote the mean ± s.e.m.

Hi-C studies on BRD4 depletion) yielded a significant, but relatively attenuated, increase in center-to-center distances (Extended Data Fig. 6e). Thus, Oligopaint FISH probes targeted to three loci validated our Hi-C results, indicating a critical role for BRD4 in maintaining TAD interactions.

To further examine the role of the BRD4–NIPBL interaction in mediating genome folding, we introduced green fluorescent protein (GFP)-fused NIPBL-binding-defective hBRD4 constructs (BRD4–dET, –L630W and –V634W) into dTAG–BRD4 mESCs (in a manner identical to Fig. 3f). We confirmed GFP expression in most cells (Extended Data Fig. 6f). Subsequently, we depleted

endogenous BRD4 for 4.5 h and performed FISH for the regions indicated in Fig. 5a (Fig. 5c). Wild-type GFP–hBRD4 maintained normal probe-to-probe distance; however, each NIPBL-binding defective mutant increased center-to-center distances compared with wild-type GFP–hBRD4 or control cells. The enrichment of chromatin-bound GFP–hBRD4 was comparable at two different sites in the regions painted by FISH probes (Extended Data Fig. 6g). Individual probe geometry was not affected (Extended Data Fig. 6c). Collectively, these data further support a model in which BRD4 promotes normal genome folding through an NIPBL interaction via the ET domain.
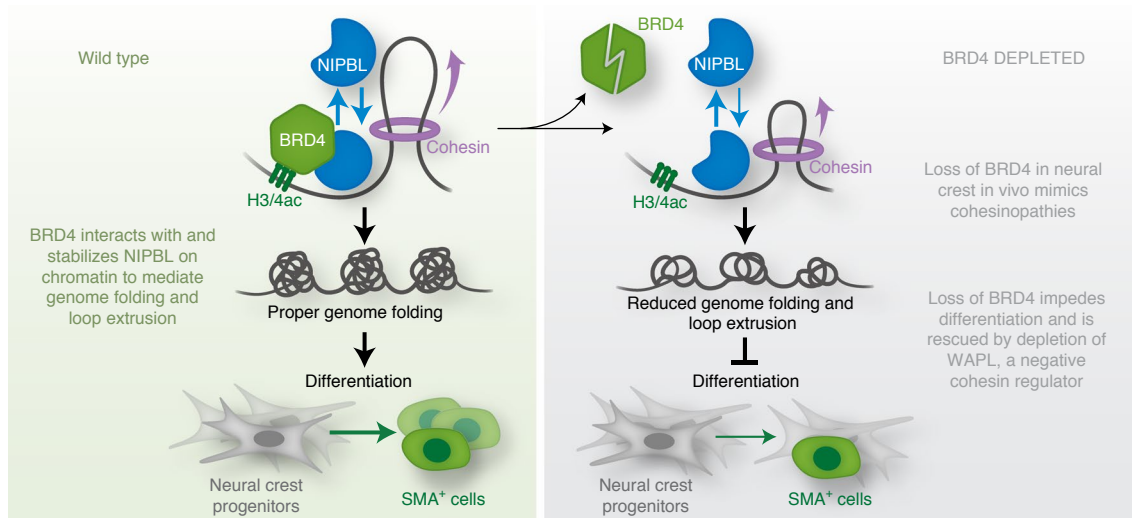
**Fig. 8 | Model depicting proposed mechanism of action of BRD4 to stabilize NIPBL on chromatin to maintain chromatin interactions and loop extrusion.** Loss of BRD4 reduces NIPBL occupancy and leads to loss of genome folding and neural crest differentiation. Restoration of the mechanisms underlying genome folding restores neural crest progenitor differentiation.

The ability of NIPBL to regulate genome folding is attributed to two, probably linked, mechanisms: facilitating loading of cohesin, which in turn extrudes chromatin loops to mediate interactions between distal regions[59,60]. Chromatin fractionation followed by western blotting for cohesin ring components on BRD4 depletion did not reveal a change in the amount of cohesin bound to chromatin (Extended Data Fig. 7a). Therefore, we reanalyzed our Hi-C data to specifically capture features associated with loop extrusion. In particular, an asymmetric enrichment signal on one edge of a TAD forms a 'stripe'. The stripe is postulated to form via a loop extrusion process and reflect an interaction of a single locus with a continuous segment of the genome. Consistent with previous reports[61], NIPBL and RAD21 occupancy was enriched at stripe anchors in DMSO-treated dTAG–BRD4 mESCs (Extended Data Fig. 7b). BRD4 was also enriched at stripe anchors (Extended Data Fig. 7b). Loss of *Nipbl* results in a dramatic reduction in loop extrusion using in vitro reconstitution assays[15]; consistently, we observed an approximately threefold reduction in the number of stripes on BRD4 depletion (Extended Data Fig. 7c,d and Supplementary Table 3). Stripenn[62], an image-processing algorithm developed by our group, calculates a stripe score that integrates the contrast across the stripe and its background, pixel continuity within the stripe and the median pixel intensity of the stripe. Regions identified as stripes in DMSO cells had a reduced stripe score and median pixel intensity on BRD4 depletion (Extended Data Fig. 7e). We then assessed NIPBL occupancy in stripe domains and at regions previously identified as RAD21–NIPBL co-bound peaks, posited to represent cohesin-loading sites[61]. NIPBL occupancy was decreased at both RAD21–NIPBL co-bound peaks and NIPBL peaks within stripe domains (Extended Data Fig. 7f,g). Furthermore, we assessed RAD21 occupancy from duplicate samples using CUT&RUN, which were processed as above. We observed a moderate reduction in RAD21 occupancy at RAD21–NIPBL peaks and at RAD21 peaks within stripe domains on BRD4 depletion (Extended Data Fig. 7h,i). These data suggest that BRD4-mediated NIPBL maintenance on chromatin impacts loop extrusion and RAD21 occupancy at RAD21–NIPBL sites and along stripe domains. Taken together, our data reveal that BRD4 mediates genome folding and higher-order chromatin organization.

**Integrating transcription changes with altered architecture.** BRD4 is a well-characterized transcription regulator[23], and we

sought to understand the relationship between the architectural changes we observed and transcriptional changes anticipated on BRD4 depletion. Therefore, we assessed transcriptional dynamics in DMSO- and degron-treated cells using SLAM (SH-linked alkylation for the metabolic sequencing of RNA)-sequencing, a technique that measures levels of newly transcribed messenger RNA based on 4-thiouridine incorporation[63]. As expected, SLAM-seq identified more changes in transcript levels compared with total RNA-sequencing (Fig. 6a). SLAM-seq identified 1,050 downregulated genes and 388 upregulated genes on BRD4 depletion for 4.5 h ($n = 3$ replicates; $\log_2$(fold-change (FC)) > 1, false discovery rate (FDR) < 0.05; Fig. 6a and Supplementary Tables 2 and 5). In addition, cohesin subunits were not differentially expressed (Supplementary Table 5). We calculated the percentage of genes that were dysregulated in individual TADs using SLAM-seq data. Dysregulated genes were most enriched in the deciles of TADs with greater interaction frequency changes on BRD4 loss (Fig. 6b and Extended Data Fig. 7j). However, even among the TADs that lost the most interaction frequency on BRD4 loss (top 10%, $n = 480$), 66% of the TADs ($n = 317$) did not contain any dysregulated genes, whether normalized to the number of genes (Fig. 6b) or to TADs (Extended Data Fig. 7j) in each decile. Overall, we found that 3,896 TADs had no significantly dysregulated genes and 113 TADs contained no genes (Fig. 6b,c and Extended Data Fig. 7j). Furthermore, although we found an enrichment for differentially expressed genes closer to anchors of BRD4-sensitive versus BRD4-resistant loop anchors, the enrichment was not different from the underlying gene distribution (Extended Data Fig. 7k). The causal relationship between transcription and architecture is not clear[64] and, although transcription may be an important regulator of short-range gene-level contacts[65], our data indicate that local transcriptional changes across the genome are unlikely to be sufficient to drive the BRD4-dependent effects on TADs and loops revealed in the present study.

**BRD4–NIPBL interaction promotes neural crest differentiation.** Our data reveal a necessity for BRD4 in neural crest development and underscore the importance of the BRD4–NIPBL interaction in genome organization. Therefore, we sought to understand whether loss of the BRD4–NIPBL interaction was responsible for any phenotype that we observed in the neural crest BRD4 model. A subset of cardiac neural crest contributes to the smooth muscle surrounding the aortic arch arteries, and outflow tract abnormalities mediated

by aberrant neural crests are often associated with smooth muscle differentiation defects[66,67]. Smooth muscle was reduced around the aortic arch arteries of E11.5 *Brd4^f/f^,Wnt1*Cre^+^,*R26^mt-mg/+^* embryos compared with *Brd4^f/+^,Wnt1*Cre^+^,*R26^mt-mg/+^* littermates (Fig. 7a). This was accompanied by a reduction in neural-crest-derived smooth muscle around the aorta and pulmonary artery in E14.5 *Brd4^f/f^,Wnt1*Cre^+^,*R26^mt-mg/+^* embryos compared with *Brd4^f/+^,Wnt1*Cre^+^,*R26^mt-mg/+^* littermates (Fig. 7b). To validate and extend these results, we turned to an in vitro differentiation system with the aforementioned murine neural crest progenitor cell line (O9-1).

We differentiated neural crest progenitor cells into smooth muscle actin plus (SMA^+^) smooth muscle cells using established protocols[33] (Fig. 7c). SMA^+^ cells were spindle shaped with visible stress fibers. Loss of BRD4 led to a reduction of progenitor differentiation into smooth muscle (Fig. 7c and Extended Data Fig. 8a,b). Next, we depleted endogenous *Brd4* using short hairpin (sh)RNA, while simultaneously expressing wild-type or mutant versions of GFP–hBRD4 resistant to shRNA targeting murine *Brd4*. We optimized transfection and infection conditions to ensure that expression levels of GFP–hBRD4 constructs were comparable to endogenous BRD4 (Fig. 7c and Extended Data Fig. 8a). Expression of wild-type GFP–hBRD4 maintained a normal number of SMA^+^ cells despite knockdown of endogenous *Brd4* (Fig. 7c). In contrast, introduction of NIPBL-binding-defective hBRD4 mutants did not rescue smooth muscle differentiation (Fig. 7c). Expression of two smooth muscle markers, *Cnn1* and *Acta2*, largely mirrored these results (Extended Data Fig. 8c). In addition, *Brd4* knockdown did not affect *Nipbl* expression (Extended Data Fig. 8d). These data indicate that the ET domain of BRD4 is required for neural crest progenitor differentiation into smooth muscle.

Consistent with the critical nature of the BRD4–NIPBL interaction, shRNA-mediated knockdown of *Nipbl* also impeded smooth muscle differentiation (Fig. 7d and Extended Data Fig. 8e,f). To further understand whether the smooth muscle differentiation defects produced by loss of BRD4 were due to a change in cohesin function, we sought to rescue differentiation by manipulating other cohesin regulators. A previous study demonstrated that changes in genome organization, including chromatin looping, resulting from NIPBL depletion, can be partially rescued by simultaneous depletion of WAPL, a negative cohesin regulator[25–28]. We found that simultaneous depletion of WAPL and NIPBL rescued the percentage of SMA^+^ cells differentiated from neural crest progenitors compared with NIPBL depletion alone (loss of WAPL alone had a relatively minor effect; Fig. 7d and Extended Data Fig. 8e,f), suggesting that NIPBL promotes smooth muscle differentiation by modulating cohesin function. Strikingly, simultaneous depletion of WAPL and BRD4 also rescued the percentage of SMA^+^ cells differentiated from neural crest progenitors compared with BRD4 depletion alone (Fig. 7d and Extended Data Fig. 8e). SMA^+^ cells adopted the typical morphology of spindle-shaped smooth muscle cells with visible stress fibers (Fig. 7d, insets), and expression of *Cnn1* and *Acta2* was consistent with these results (Extended Data Fig. 8g,h). Taken together, these studies suggest that BRD4 regulates genome folding through NIPBL binding, and our data are consistent with a critical functional role for this interaction in neural crest differentiation into smooth muscle cells.

## Discussion

BRD4 has been described as a 'cellular Swiss army knife', with the ability to mediate transcriptional pause release, act as a histone acetyltransferase, bind regulatory elements and recruit transcriptional machinery[23]. We reveal yet another role: BRD4 is a positive mediator of NIPBL and thereby maintains genome folding (Fig. 8). Acute loss of BRD4 weakens loop and intra-TAD interactions at specific areas across the genome and the architectural defects are at least partially attributed to a loss of BRD4–NIPBL interaction.

Accordingly, loss of BRD4 in neural crest cells in vivo phenocopies mutations in *NIPBL*, which are also often observed in human cohesinopathies. The ability to acutely degrade BRD4 in less than a cell cycle in a nondifferentiating pool of cells allowed for assessment of BRD4 loss independent of biases arising from changes in cellular identity. Extending these findings, our data suggest that one physiological role of the BRD4–NIPBL interaction is to mediate normal smooth muscle differentiation of neural crest cells. Even more striking, depletion of the negative cohesin regulator WAPL is sufficient to rescue smooth muscle differentiation in cells with BRD4 depletion. This rescue further demonstrates the critical role that BRD4 plays in mediating cohesin function. Together, the present study illustrates the functional relevance of genome folding, and specifically the importance of properly balancing the positive and negative effectors of cohesin function in cellular differentiation. Due to space constraints, we discuss the relevance of our data on understanding the cellular basis of cohesinopathies and the implications for developmental competence in the Supplementary Discussion. We also place our findings in the context of recent studies depleting cohesin (and related) proteins and how our data support and extend the loop extrusion model in the Supplementary Discussion.

## Online content

Any methods, additional references, Nature Research reporting summaries, source data, extended data, supplementary information, acknowledgements, peer review information; details of author contributions and competing interests; and statements of data and code availability are available at https://doi.org/10.1038/s41588-021-00934-8.

## References

1. Mayor, R. & Theveneau, E. The neural crest. *Development* **140**, 2247–2251 (2013).
2. Tang, W. & Bronner, M. E. Neural crest lineage analysis: from past to future trajectory. *Development* **147**, dev193193 (2020).
3. Stoller, J. Z. & Epstein, J. A. Cardiac neural crest. *Semin. Cell Dev. Biol.* **16**, 704–715 (2005).
4. Vega-Lopez, G. A., Cerrizuela, S., Tribulo, C. & Aybar, M. J. Neurocristopathies: new insights 150 years after the neural crest discovery. *Dev. Biol.* **444**, S110–S143 (2018).
5. Andrey, G. & Mundlos, S. The three-dimensional genome: regulating gene expression during pluripotency and development. *Development* **144**, 3646–3658 (2017).
6. Rowley, M. J. & Corces, V. G. Organizational principles of 3D genome architecture. *Nat. Rev. Genet.* **19**, 789–800 (2018).
7. Rao, S. S. P. et al. A 3D map of the human genome at kilobase resolution reveals principles of chromatin looping. *Cell* **159**, 1665–1680 (2014).
8. Rao, S. S. P. et al. Cohesin loss eliminates all loop domains. *Cell* **171**, 305–320.e24 (2017).
9. Wutz, G. et al. Topologically associating domains and chromatin loops depend on cohesin and are regulated by CTCF, WAPL, and PDS5 proteins. *EMBO J.* **36**, 3573–3599 (2017).
10. Kline, A. D. et al. Diagnosis and management of Cornelia de Lange syndrome: first international consensus statement. *Nat. Rev. Genet.* **19**, 649–666 (2018).
11. Piché, J., Vliet, P. P. V., Pucéat, M. & Andelfinger, G. The expanding phenotypes of cohesinopathies: one ring to rule them all! *Cell Cycle* **18**, 2828–2848 (2019).
12. Chatfield, K. C. et al. Congenital heart disease in Cornelia de Lange syndrome: phenotype and genotype analysis. *Am. J. Med. Genet. A* **158A**, 2499–2505 (2012).
13. Ciosk, R. et al. Cohesin's binding to chromosomes depends on a separate complex consisting of Scc2 and Scc4 proteins. *Mol. Cell* **5**, 243–254 (2000).
14. Tonkin, E. T., Wang, T.-J., Lisgo, S., Bamshad, M. J. & Strachan, T. NIPBL, encoding a homolog of fungal Scc2-type sister chromatid cohesion proteins and fly Nipped-B, is mutated in Cornelia de Lange syndrome. *Nat. Genet.* **36**, 636–641 (2004).
15. Davidson, I. F. et al. DNA loop extrusion by human cohesin. *Science* **366**, 1338–1345 (2019).

16. Kim, Y., Shi, Z., Zhang, H., Finkelstein, I. J. & Yu, H. Human cohesin compacts DNA by loop extrusion. *Science* **366**, 1345–1349 (2019).

17. Schwarzer, W. et al. Two independent modes of chromatin organization revealed by cohesin removal. *Nature* **551**, 51–56 (2017).

18. Smith, T. G. et al. Neural crest cell-specific inactivation of Nipbl or Mau2 during mouse development results in a late onset of craniofacial defects. *genesis* **52**, 687–694 (2014).

19. Alesi, V. et al. Confirmation of BRD4 haploinsufficiency role in Cornelia de Lange-like phenotype and delineation of a 19p13.12p13.11 gene contiguous syndrome. *Ann. Hum. Genet.* **83**, 100–109 (2019).

20. Olley, G. et al. BRD4 interacts with NIPBL and BRD4 is mutated in a Cornelia de Lange-like syndrome. *Nat. Genet.* **50**, 329–332 (2018).

21. Filippakopoulos, P. et al. Selective inhibition of BET bromodomains. *Nature* **468**, 1067–1073 (2010).

22. Luna-Peláez, N. et al. The Cornelia de Lange syndrome-associated factor NIPBL interacts with BRD4 ET domain for transcription control of a common set of genes. *Cell Death Dis.* **10**, 548 (2019).

23. Devaiah, B. N., Gegonne, A. & Singer, D. S. Bromodomain 4: a cellular Swiss army knife. *J. Leukoc. Biol.* **100**, 679–686 (2016).

24. Beliveau, B. J. et al. Versatile design and synthesis platform for visualizing genomes with Oligopaint FISH probes. *Proc. Natl Acad. Sci. USA* **109**, 21301–21306 (2012).

25. Haarhuis, J. H. I. et al. The cohesin release factor WAPL restricts chromatin loop extension. *Cell* **169**, 693–707.e14 (2017).

26. Tedeschi, A. et al. Wapl is an essential regulator of chromatin structure and chromosome segregation. *Nature* **501**, 564–568 (2013).

27. Liu, N. Q. et al. WAPL maintains a cohesin loading cycle to preserve cell-type-specific distal gene regulation. *Nat. Genet.* **53**, 100–109 (2021).

28. Kueng, S. et al. Wapl controls the dynamic association of cohesin with chromatin. *Cell* **127**, 955–967 (2006).

29. Padmanabhan, A. et al. BRD4 (bromodomain-containing protein 4) interacts with GATA4 (GATA binding protein 4) to govern mitochondrial homeostasis in adult cardiomyocytes. *Circulation* **142**, 2338–2355 (2020).

30. Lee, J.-E. et al. Brd4 binds to active enhancers to control cell identity gene induction in adipogenesis and myogenesis. *Nat. Commun.* **8**, 2217 (2017).

31. Jiang, X., Rowitch, D. H., Soriano, P., McMahon, A. P. & Sucov, H. M. Fate of the mammalian cardiac neural crest. *Development* **127**, 1607–1616 (2000).

32. Santos, R. et al. Conditional creation and rescue of Nipbl-deficiency in mice reveals multiple determinants of risk for congenital heart defects. *PLoS Biol.* **14**, e2000197 (2016).

33. Ishii, M. et al. A stable cranial neural crest cell line from mouse. *Stem Cells Dev.* **21**, 3069–3080 (2012).

34. Zengerle, M., Chan, K.-H. & Ciulli, A. Selective small molecule induced degradation of the BET bromodomain protein BRD4. *ACS Chem. Biol.* **10**, 1770–1777 (2015).

35. Watrin, E. et al. Human Scc4 Is required for cohesin binding to chromatin, sister-chromatid cohesion, and mitotic progression. *Curr. Biol.* **16**, 863–874 (2006).

36. Zhang, Q. et al. Structural mechanism of transcriptional regulator NSD3 recognition by the ET domain of BRD4. *Structure* **24**, 1201–1208 (2016).

37. Shen, C. et al. NSD3-Short is an adaptor protein that couples BRD4 to the CHD8 chromatin remodeler. *Mol. Cell* **60**, 847–859 (2015).

38. Jung, M. et al. Affinity map of bromodomain protein 4 (BRD4) Interactions with the histone H4 Ttail and the small molecule inhibitor JQ1*. *J. Biol. Chem.* **289**, 9304–9319 (2014).

39. Crowe, B. L. et al. Structure of the Brd4 ET domain bound to a C-terminal motif from γ-retroviral integrases reveals a conserved mechanism of interaction. *Proc. Natl Acad. Sci. USA* **113**, 2086–2091 (2016).

40. Konuma, T. et al. Structural mechanism of the oxygenase JMJD6 recognition by the extraterminal (ET) domain of BRD4. *Sci. Rep.* **7**, 16272 (2017).

41. Hnisz, D. et al. Super-enhancers in the control of cell identity and disease. *Cell* **155**, 934–947 (2013).

42. Kagey, M. H. et al. Mediator and cohesin connect gene expression and chromatin architecture. *Nature* **467**, 430–435 (2010).

43. Nabet, B. et al. The dTAG system for immediate and target-specific protein degradation. *Nat. Chem. Biol.* **14**, 431–441 (2018).

44. Fernandez-Alonso, R. et al. Brd4–Brd2 isoform switching coordinates pluripotent exit and Smad2-dependent lineage specification. *EMBO Rep.* **18**, 1108–1122 (2017).

45. White, J. & Dalton, S. Cell cycle control of embryonic stem cells. *Stem Cell Rev.* **1**, 131–138 (2005).

46. Skene, P. J. & Henikoff, S. An efficient targeted nuclease strategy for high-resolution mapping of DNA binding sites. *eLife* **6**, e21856 (2017).

47. Nabet, B. et al. Rapid and direct control of target protein levels with VHL-recruiting dTAG molecules. *Nat. Commun.* **11**, 4687 (2020).

48. Creyghton, M. P. et al. Histone H3K27ac separates active from poised enhancers and predicts developmental state. *Proc. Natl Acad. Sci. USA* **107**, 21931–21936 (2010).

49. Lieberman-Aiden, E. et al. Comprehensive mapping of long-range interactions reveals folding principles of the human genome. *Science* **326**, 289–293 (2009).

50. Servant, N. et al. HiC-Pro: an optimized and flexible pipeline for Hi-C data processing. *Genome Biol.* **16**, 259 (2015).

51. Dixon, J. R. et al. Topological domains in mammalian genomes identified by analysis of chromatin interactions. *Nature* **485**, 376–380 (2012).

52. Nora, E. P. et al. Spatial partitioning of the regulatory landscape of the X-inactivation centre. *Nature* **485**, 381–385 (2012).

53. Bonev, B. et al. Multiscale 3D genome rewiring during mouse neural development. *Cell* **171**, 557–572.e24 (2017).

54. Cao, Y. et al. Accurate loop calling for 3D genomic data with cLoops. *Bioinformatics* **36**, 666–675 (2020).

55. Mumbach, M. R. et al. HiChIP: efficient and sensitive analysis of protein-directed genome architecture. *Nat. Methods* **13**, 919–922 (2016).

56. Zhang, H. et al. Chromatin structure dynamics during the mitosis-to-G1 phase transition. *Nature* **576**, 158–162 (2019).

57. Gong, Y. et al. Stratification of TAD boundaries reveals preferential insulation of super-enhancers by strong boundaries.*Nat. Commun.* **9**, 542 (2018).

58. Luppino, J. M. et al. Cohesin promotes stochastic domain intermingling to ensure proper regulation of boundary-proximal genes. *Nat. Genet.* **52**, 840–848 (2020).

59. Fudenberg, G. et al. Formation of chromosomal domains by loop extrusion. *Cell Rep.* **15**, 2038–2049 (2016).

60. Sanborn, A. L. et al. Chromatin extrusion explains key features of loop and domain formation in wild-type and engineered genomes. *Proc. Natl Acad. Sci. USA* **112**, E6456–E6465 (2015).

61. Vian, L. et al. The energetics and physiological impact of cohesin extrusion. *Cell* **173**, 1165–1178.e20 (2018).

62. Yoon, S. & Vahedi, G. Stripenn detects architectural stripes from chromatin conformation data using computer vision. Preprint at *bioRxiv* https://doi.org/2021.04.16.440239 (2021).

63. Herzog, V. A. et al. Thiol-linked alkylation of RNA to assess expression dynamics. *Nat. Methods* **14**, 1198–1204 (2017).

64. Hug, C. B., Grimaldi, A. G., Kruse, K. & Vaquerizas, J. M. Chromatin architecture emerges during zygotic genome activation independent of transcription. *Cell* **169**, 216–228.e19 (2017).

65. Hsieh, T.-H. S. et al. Resolving the 3D landscape of transcription-linked mammalian chromatin folding. *Mol. Cell* **78**, 539–553.e8 (2020).

66. High, F. A. & Epstein, J. A. The multifaceted role of Notch in cardiac development and disease. *Nat. Rev. Genet.* **9**, 49–61 (2008).

67. High, F. A. et al. An essential role for Notch in neural crest during cardiovascular development and smooth muscle differentiation. *J. Clin. Invest.* **117**, 353–363 (2007).

## Methods

**Mice.** *Brd4* floxed mice were obtained from K. Ozato's laboratory[30] and *Wnt1*Cre mice were obtained from Jackson Laboratories (catalog no. 022137). *R26*[mt-mg] mice were also obtained from Jackson Laboratories[68]. Mice were maintained on mixed CD1/B6/129 genetic backgrounds. Littermate embryos were analyzed in all experiments unless otherwise noted. The Institutional Animal Care and Use Committee approved all animal protocols.

**Tissue immunohistochemistry and immunofluorescence.** Mice were dissected and embryos were harvested at E11.5, E12.5, E14.5, E16.5 and E17.5. All embryos were fixed in 2% paraformaldehyde (PFA) in phosphate-buffered saline (PBS; Sigma-Aldrich, catalog no. P6148) overnight at 4 °C on a tilting shaker set at low speed. After fixation, the embryos were dehydrated with an ethanol gradient (30% ethanol for 2 h, 50% ethanol for 2 h, 70% ethanol for 2 h, 95% ethanol overnight and 100% ethanol overnight). Dehydrated embryos were perforated, cleared with xylene, embedded in paraffin blocks and sectioned into 7-μm-thick segments.

Gross tissue morphology was examined by hematoxylin and eosin (H&E) staining following standardized methods of the University of Pennsylvania Histology and Gene Expression Co-Op (https://www.med.upenn.edu/cvi/histology-and-gene-expression-co-op.html)[69]. Collagen and extracellular matrix deposition, bone mineralization and smooth muscle morphology were assessed by Masson Trichrome Staining according to the standard protocol of the University of Pennsylvania Histology and Gene Expression Co-Op. All slides were imaged at ×2 or ×4 magnification on the Nikon Eclipse 80i fluorescence microscope.

Sections analyzed by immunofluorescence (IF) were stained per the optimized and standardized methods of the University of Pennsylvania Histology and Gene Expression Co-Op. Briefly, slides were brought to room temperature, deparaffinized with xylene and rehydrated through a series of steps (100% ethanol for 2 min, 95% ethanol for 2 min and ddH₂O for 2 min twice). Tissue sections were blocked and permeabilized in 10% normal serum in PBS + 0.5% Tween-20, after which the slides were incubated with designated primary antibodies overnight at 40 °C. After four washes with 0.1% PBS–Tween-20 for 5 min at room temperature, corresponding secondary antibodies were added, incubated for an hour at room temperature and washes were performed as above. Slides were mounted with VectaShield with DAPI (Vector Laboratories, catalog no. H-2000) mounting medium and scanned on the Aperio ScanScope IF (Leica Biosystems) at ×20 magnification. Areas populated by neural crest derivatives were manually outlined and the number of DAPI⁺, Wnt1⁺(GFP⁺) and phospho-histone H3⁺ cells were quantified using certain features on Image J. At least two embryos (approximately 30–37 frontal sections in total) were quantified per genotype. Proliferation indices were calculated as percentage of DAPI⁺ and Wnt1⁺ cells at E11.5. Statistical significance between genotypes was calculated using GraphPad Prism v.9 (GraphPad Software Inc.).

Primary antibodies and dilutions used are as follows: goat polyclonal anti-GFP (1:100, Abcam, catalog no. ab6673, lot no. GR3213188-14), rabbit polyclonal anti-BRD4 (1:2,000, Bethyl, catalog no. A301-985A100, lot no. 7), rabbit polyclonal anti-phospho-histone H3 (Ser10) (1:20, Cell Signaling, catalog no. 9710L) and mouse monoclonal anti-α smooth muscle actin (SMA; 1:200, Sigma-Aldrich, catalog no. A5228, lot no. 065M4762V). Antigen retrieval was used for all primary antibodies except for anti-α SMA. Secondary antibodies and dilutions used are as follows: Alexa Fluor-555 donkey anti-rabbit immunoglobulin (Ig)G(H+L) (1:250, Invitrogen, catalog no. A31572, lot no. 2088692) and Alexa Fluor-488 donkey anti-goat IgG(H+L) (1:250, Invitrogen, catalog no. A11055, lot no. 2059218).

**Cell culture.** HEK293T cells were purchased from American Type Culture Collection (ATCC, catalog no. CRL-11268) and maintained at 37 °C in 20% O₂ and 5% CO₂ in Dulbecco's modified Eagle's medium (DMEM) supplemented with 10% fetal bovine serum (FBS) and 1% penicillin–streptomycin. The mESCs (ATCC, catalog no. CRL-1934) were maintained at 37 °C in 20% O₂ and 5% CO₂ on gelatin-coated plates in knockout DMEM (Gibco, catalog no. 10829018), 10% knockout serum replacement (Gibco, catalog no. 10828028), 1% FBS (Hyclone, catalog no. SH30070.03), 1× non-essential amino acids (Gibco, catalog no. 11140050), 2 mM L-glutamine (Gibco, catalog no. 25030081), 1% ITS-X supplement (Gibco, catalog no. 51500056), 55 μM β-mercaptoethanol (Gibco, catalog no. 21985023), 1×10³ units ml⁻¹ of recombinant mouse leukemia inhibitory factor (LIF; Millipore, catalog no. ESG1107), 3 μM glycogen synthase kinase-β (GSK-β) inhibitor CHIR99021 (Reprocell, catalog no. 04-0004-02), 1 μM mitogen activated protein kinase inhibitor PD-0325901 (Reprocell, catalog no. 04-0006-02) and 1% penicillin–streptomycin. For the O9-1 neural crest cell line (Sigma-Aldrich, catalog no. SCC049), cells were cultured in basal medium (DMEM, 15% FBS, 0.1 mM non-essential amino acids and 1 mM sodium pyruvate (Gibco, catalog no. 11360070), 55 μM β-mercaptoethanol, 100 U ml⁻¹ of penicillin, 100 μg ml⁻¹ of streptomycin and 2 mM L-glutamine) previously conditioned by STO feeder cells for 24 h. The medium was filtered using a 0.22-μm PES membrane (Millipore, catalog no. SCGP00525) and supplemented with 25 ng ml⁻¹ of basic fibroblast growth factor (R&D Systems, catalog no. 233-FB-025) and 1×10³ units ml⁻¹ of recombinant mouse LIF. To induce smooth muscle cell differentiation, O9-1 cells were cultured in differentiation medium (DMEM, 10% FBS, 100 U ml⁻¹ of penicillin and 100 μg ml⁻¹ of streptomycin) for 2 d (for real-time quantitative (q)

PCR and IF experiments) and 3 d (for western blotting experiments) to assess differentiation markers; dTAG-13 (Sigma-Aldrich, catalog no. SML2601), dTAGᵛ-1 (a gift from N. Grey's laboratory) and MZ3 (a gift from T. Ciulli's laboratory) were treated at appropriate concentrations and times as indicated in the figures.

**Immunofluorescence.** Cells were fixed with 2% (O9-1 cells) or 4% (mESCs) PFA (Electron Microscopy Sciences, catalog no. 15710) for 10 min, washed twice with PBS for 5 min, permeabilized with 0.5% Triton X-100/PBS for 5 min and washed twice with PBS for 5 min. All steps were performed at room temperature. Cells were then incubated with blocking solution (3% bovine serum albumin (BSA) and 0.02% Tween-20–PBS) for 1 h at room temperature, followed by overnight incubation with primary antibody in blocking solution at 4 °C. The antibodies used were anti-BRD4 (1:100, Bethyl Laboratories, catalog no. A301-985A100, lot no. 7), anti-GFP (1:100, Abcam, catalog no. ab290), anti-OCT4 (1:200, Abcam, catalog no. ab19857, lot no. GR3173193-1) and Cy3-conjugated SMA antibody (1:5,000, anti-actin α-smooth muscle-Cy3, Sigma, catalog no. C6198). The following day, cells were washed three times with 0.02% Tween-20–PBS for 5 min, and incubated with secondary antibodies (goat anti-rabbit IgG secondary antibody, Alexa Fluor Plus 488 (1:1,000, Thermo Fisher Scientific, catalog no. A32731, lot no. VG302077) and Alexa Fluor-555 (1:1,000, Thermo Fisher Scientific, catalog no. A32732, lot no. VG308859) and goat anti-mouse IgG secondary antibody, Alexa Fluor Plus 488 (1:1,000, Thermo Fisher Scientific, catalog no. A10680, lot no. 2064014) and Alexa Fluor-555 (1:1,000, Thermo Fisher Scientific, catalog no. A32727, lot no. UL287768)) for 2 h at room temperature. Cells were washed three times with 0.1% Tween-20–PBS (PBST) for 5 min. Nuclear staining was carried out with incubation of DAPI (1:5,000 in PBS), for 5 min, followed by three 5-min washes in PBST. Samples were mounted with SlowFade Gold Antifade Mountant (Thermo Fisher Scientific, catalog no. S36936). Images were obtained with a Leica SP8 confocal microscope using ×63/1.40 oil objective or with a Leica widefield DMi8 microscope using a ×10 objective. For SMA⁺ and BRD4⁺ cell quantification, we used at least three biological replicates per condition, and imaged more than three random fields per sample. The images were then semiautomatically processed in ImageJ v.1.53c by thresholding each antibody signal and quantifying unique segmentations per nuclear mask. The statistical analysis of the cell counts was performed in GraphPad Prism v.9.

**Oligopaint FISH.** Adherent dTAG–BRD4 cells were harvested using Accutase solution (Sigma-Aldrich, catalog no. A6964), washed twice in PBS for 5 min, fixed for 10 min in 4% PFA (Thermo Fisher Scientific, catalog no. 15713S) in PBS with 0.05% Tween-20, followed by three washes in PBS for 5 min each. Cells were then settled on poly(L-lysine)-treated glass slides for 30 min at room temperature and stored in PBS at 4 °C until ready to use. Hybridization steps were performed directly on the slides, as previously described[58] with some modifications. Cells were permeabilized in 0.5% Triton/PBS for 15 min. Slides were then incubated in 2× SSCT (0.3 M NaCl, 0.03 M sodium citrate and 0.1% Tween-20) for 5 min at room temperature, 2× SSCT/50% formamide (Thermo Fisher Scientific, catalog no. BP227500) for 5 min at room temperature, and 2× SSCT/50% formamide for 20 min at 60 °C. Hybridization mix (50 μM Oligopaint FISH probes (50 pmol of probes in 25-μl total volume), 10% dextran sulfate, 2× SSCT/50% formamide, 4% poly(vinylsulfonic acid) (PVSA), 5.6 mM dNTPs and 10 μg RNase) was added to the slides and covered with a coverslip. Slides were then denatured on a heat block at 80 °C for 30 min, and incubated at 37 °C overnight in a humidified chamber. The next day, the coverslip was removed, and the slides were washed in 2× SSCT at 60 °C for 15 min, 2× SSCT at room temperature for 10 min and 0.2× SSC at room temperature for 10 min. Next, hybridization buffer (10% dextran sulfate, 2× SSCT, 10% formamide and 4% PVSA) containing secondary probes conjugated to fluorophores (10 pmol per 25-μl buffer) was added to the slides and covered with coverslips. Slides were placed in a humidified chamber and incubated for 2 h at room temperature. Slides were washed in 2× SSCT at 60 °C for 15 min, 2× SSCT at room temperature for 10 min and 0.2× SSC at room temperature for 10 min, and then the DNA was stained with Hoechst (1:10,000 in 2× SSC) for 5 min. Slides were then mounted in SlowFade Gold Antifade (Thermo Fisher Scientific, catalog no. S36936).

**CUT&RUN.** The CUT&RUN protocol was performed in triplicate for BRD4 and NIPBL and in duplicate for H3K27ac and RAD21, and performed as previously described[70] with modifications. Briefly, 5×10⁶ mESCs per well were treated with 500 nM dTAG-13 or DMSO and harvested at 4.5 h. Following treatment, cells were harvested via gentle agitation after incubation with Accutase for 5 min, and collected via centrifugation at 300g for 3 min at 4 °C. The cells were washed twice with ice-cold PBS and nuclei were isolated with nuclear extraction buffer (20 mM 4-(2-hydroxyethyl)-1-piperazine-ethanesulfonic acid (Hepes)-KOH, pH 7.9, 10 mM KCl, 0.5 mM spermidine (Sigma-Aldrich, catalog no. 05292-1ml-F), 0.1% Triton X-100, 20% glycerol and 1× protease and phosphatase inhibitor (Thermo Fisher Scientific, catalog no. 78442)). To help nuclear capture, isolated nuclei were incubated with activated concanavalin A beads (Bangs Laboratories, catalog no. Bp531) for 15 min at room temperature, followed by incubation with the desired primary antibody (1:100 dilution) overnight. Any unbound antibody was washed away using wash buffer (20 mM Hepes-NaOH, pH 7.5, 150 mM NaCl, 0.5 mM

spermidine and 1× protease phosphatase inhibitor) for a total of two washes. Supernatant was discarded via bead liquid separation using a magnetic stand and pA-MNase was added at a final concentration of 700 ng ml$^{-1}$ (batch 6: stock concentration: 143 µg ml$^{-1}$) and the complex was incubated for 1 h at 4 °C. After incubation, the bound complexes were washed twice with wash buffer and placed in a 0 °C metal block for 5 min to pre-chill the tubes. To activate pA-MNase, CaCl$_2$ was added to the pre-chilled bound complexes at a final concentration of 2 mM and incubated in the 0 °C metal block for 30 min. The digestion reaction was neutralized by the addition of an equal volume of 2× STOP buffer (200 mM NaCl, 20 mM ethylenediaminetetraacetic acid (EDTA), 4 mM (ethylenebis(oxonitrilo)) tetra-acetate, 50 µg ml$^{-1}$ of RNase A, 40 µg ml$^{-1}$ of glycogen and 100 pg ml$^{-1}$ of heterologous spike in DNA) followed by incubation at 37 °C for 10 min to release cleaved fragments of DNA. The targeted protein–DNA complex was released via centrifugation at 16,000g for 5 min, and the supernatant was collected and transferred to freshly labeled 1.7-ml tubes. Depending on whether the targeted proteins were nucleosomal or transcription factors, the digested DNA was purified either via a spin column or phenol–chloroform. For H3K27ac, a method of spin column extraction (Macherey–Nagel, catalog no. 740609.250) was followed according to the manufacturer's instructions to recover large DNA–protein complexes. To enrich for smaller fragments occupied by nonhistone proteins (BRD4, NIPBL and RAD21), a phenol–chloroform extraction protocol was followed as briefly described. The supernatant was decanted into a fresh tube to which 10% sodium dodecylsulfate (final concentration 0.1%) and proteinase K (final concentration 20 mg ml$^{-1}$) were added and mixed by inversion, followed by incubation for 10 min at 70 °C. Post-incubation, a phenol–chloroform–isoamyl alcohol mix was added to the solution and vortexed at full speed to mix. The solution was transferred to a phase lock tube, centrifuged at 16,000g for 5 min and inverted 10 times after the addition of chloroform, followed by another round of centrifugation at 16,000g for 5 min. The supernatant was transferred to a fresh tube containing glycogen (final concentration 20 µg ml$^{-1}$) and DNA was precipitated via the addition of 100% ethanol. The samples were incubated on ice for 10 min and subsequently centrifuged at 16,000g and 4 °C. Excess liquid was carefully discarded, 1 ml of ethanol was added to the pellet and the tubes were mixed by inverting. Samples were centrifuged once again at 16,000g and 4 °C. The supernatant was carefully discarded, and the pellet was air dried for 10 min and resuspended in a desired amount of TE buffer (1 mM Tris-HCl, pH 8, 0.1 mM EDTA). DNA concentration after both methods of extraction was estimated using the Qubit and quality was assessed before library preparation with the Agilent BioAnalyzer 2100 (Agilent Technologies) using the High Sensitivity DNA Kit (Agilent Technologies, catalog no. 5067-4626). The following antibodies were used: rabbit polyclonal anti-BRD4 (Bethyl Laboratories, catalog no. A301-985A100, lot no. 7), rabbit polyclonal anti-NIPBL (Bethyl Laboratories, catalog no. A301–779, lot no. 4), rabbit polyclonal anti-H3K27ac (Abcam, catalog no. Ab4729), rabbit polyclonal anti-RAD21 (Abcam, catalog no. Ab992) and normal rabbit IgG (Cell Signaling, catalog no. 2729S).

**SLAM-seq.** The SLAM-seq protocol was carried out as described in the SLAM-seq Anabolic Kinetics Kit user guide (Lexogen, catalog no. 061.24) with modifications. Briefly, mESCs were seeded in 0.1% bovine gelatin-coated (Sigma-Aldrich, catalog no. G9391-500g), six-well plates approximately 2 d before 4-thiouridine labeling to attain an optimum confluency of around 70–80% (~2 × 10$^6$ cells). All conditions were set up in triplicate. On the day of labeling, mESC medium was aspirated and refreshed with pre-warmed mESC growth medium containing either 500 nM dTAG-13 or DMSO to pre-establish acute degradation of BRD4. The time course for BRD4 degradation was set at 4.5 h; 15 min into the time course, newly synthesized RNA was labeled via the addition of 4-thiouridine to all wells, including controls, at a final concentration of 500 µM per well, and metabolic labeling was continued until the end of the time course. For the 4.5-h time point, 4-thiouridine medium was refreshed after 3 h to continue efficient labeling. At the respective time points, medium was aspirated and mESCs were harvested after the addition of 400 µl of Accutase. The single-cell suspension from each well was transferred into corresponding tubes and centrifuged at 2,500 r.p.m. for 5 min to pellet cells. The cell pellet was washed twice with ice-cold 1× PBS and RNA extraction was carried out using the RNeasy Plus kit (QIAGEN, catalog no. 74134). The recommended amount of reducing agent (as indicated in the manufacturer's protocol) was added to all extraction buffers to maintain a reducing environment during extraction. Total RNA, 8 µg, was alkylated via treatment with 10 mM iodoacetamide at 50 °C for 5 min under optimal reaction conditions, and purified by ethanol precipitation. Iodoacetamide-fixed RNA concentrations were estimated using Nanodrop, and ~300 ng µl$^{-1}$ of alkylated RNA per sample was sent to Lexogen for downstream processing and sequencing. On arrival, RNA concentration and quality were assessed via Nanodrop. Subsequently, RNA integrity was assessed on the Agilent Bioanalyzer (Agilent Technologies), before library preparation, using the RNA 6000 Nano Assay Kit (Agilent Technologies, catalog no. 5067-1511).

**In situ Hi-C.** The in situ Hi-C protocol was carried out as previously described[7] with modifications. Briefly, mESCs were seeded in 0.1% bovine gelatin-coated (Sigma-Aldrich, catalog no. G9391-500g), six-well plates approximately 3 d before harvest to attain an optimum confluency on the day of harvest. All conditions

were set up in duplicate. On the day of harvest, mESC medium was aspirated and refreshed with pre-warmed mESC growth medium containing either 500 nM dTAG-13 or DMSO to establish acute degradation of BRD4 for a time course of 4.5 h. After treatment, mESC medium was aspirated and cells were harvested following the addition of 400 µl of Accutase. The single-cell suspension from each well was transferred into its respective tube and centrifuged at 2,500 r.p.m. for 5 min. The resulting cell pellet was washed twice with ice-cold 1× PBS and aliquoted into separate tubes containing 1.5 × 10$^6$ cells each (per well/per condition). Cells were briefly centrifuged at 2,500 r.p.m. and 4 °C for 5 min and the supernatant was discarded. The cell pellet containing 1.5 × 10$^6$ cells was resuspended and crosslinked in 1% formaldehyde (Thermo Fisher Scientific, catalog no. 28906) for 12 min. The crosslinking reaction was quenched by the addition of 2.5 M glycine (final concentration 0.2 M; Thermo Fisher Scientific, catalog no. 15527013) followed by incubation for 5 min. Crosslinked cells were pelleted via centrifugation at 2,500 r.p.m. and 4 °C for 5 min and the supernatant was discarded. Cells were resuspended and washed twice with ice-cold 1× PBS to remove all traces of formaldehyde. Cell pellets were flash frozen and stored at −80 °C until required for downstream processing. Frozen cell pellets were shipped on dry ice to the Genome Technology Center at NYU Langone Health, New York. All subsequent processing, quality control and sequencing of samples were carried out at the Genome Technology Center.

**Quantification and statistical analysis.** All statistical comparisons were performed in R v.3.5.2 or GraphPad Prism v.9, as specified in the relevant figures and corresponding methods sections. Normality of the data was assessed visually with QQplots and formally using the Shapiro–Wilk test in R as indicated. Quality control of sequenced reads was performed by FastQC (https://github.com/s-andrews/FastQC) and MultiQC (https://github.com/ewels/MultiQC). Correlation between mapped reads from biological replicates was assessed in deepTools v.3.1.3 using Spearman's method.

**Reporting Summary.** Further information on research design is available in the Nature Research Reporting Summary linked to this article.

## Data availability
All data generated for this paper have been deposited at the National Center for Biotechnology Information Gene Expression Omnibus (http://www.ncbi.nlm.nih.gov/geo) and are available under accession no. GSE169516.
Mouse genome sequence mm10:
http://ftp.ebi.ac.uk/pub/databases/gencode/Gencode_mouse/release_M10/GRCm38.primary_assembly.genome.fa.gz
*Saccharomyces cerevisiae* genome sequence sacCer3: https://hgdownload.soe.ucsc.edu/goldenPath/sacCer3/bigZips/sacCer3.fa.gz
BRD4 ChIP–seq: http://dc2.cistrome.org/api/hgtext/34084/?db=mm10
NIPBL ChIP–seq: http://dc2.cistrome.org/api/hgtext/2864/?db=mm10
H3K27ac ChIP–seq: http://dc2.cistrome.org/api/hgtext/67169/?db=mm10
RAD21 ChIP–seq: http://dc2.cistrome.org/api/hgtext/39300/?db=mm10. Source data are provided with this paper.

## Code availability
OligoMiner is available at https://github.com/beliveau-lab/OligoMiner and cLoops at https://github.com/YaqiangCao/cLoops. TADtool is available at https://github.com/vaquerizaslab/tadtool and Juicer Tools at https://github.com/aidenlab/juicer. The other tools used are indicated in Methods. We utilized existing published analysis tools as indicated above. No new analysis tools were generated, and scripts employed to analyze the data using the published tools are available upon request.

## References
68. Muzumdar, M. D., Tasic, B., Miyamichi, K., Li, L. & Luo, L. A global double-fluorescent Cre reporter mouse. *genesis* **45**, 593–605 (2007).
69. Aghajanian, H. et al. Pdgfrα functions in endothelial-derived cells to regulate neural crest cells and the development of the great arteries. *Dis. Model Mech.* **10**, 1101–1108 (2017).
70. Skene, P. J., Henikoff, J. G. & Henikoff, S. Targeted in situ genome-wide profiling with high efficiency for low cell numbers. *Nat. Protoc.* **13**, 1006–1019 (2018).
71. Jones, D. T. Protein secondary structure prediction based on position-specific scoring matrices. *J. Mol. Biol.* **292**, 195–202 (1999).

## Author contributions

## Competing interests

## Additional information

**Extended data** are available for this paper at https://doi.org/10.1038/s41588-021-00934-8.

**Supplementary information** The online version contains supplementary material available at https://doi.org/10.1038/s41588-021-00934-8.

**Correspondence and requests for materials** should be addressed to Rajan Jain.

**Peer review information** *Nature Genetics* thanks the anonymous reviewers for their contribution to the peer review of this work.

**Reprints and permissions information** is available at www.nature.com/reprints.
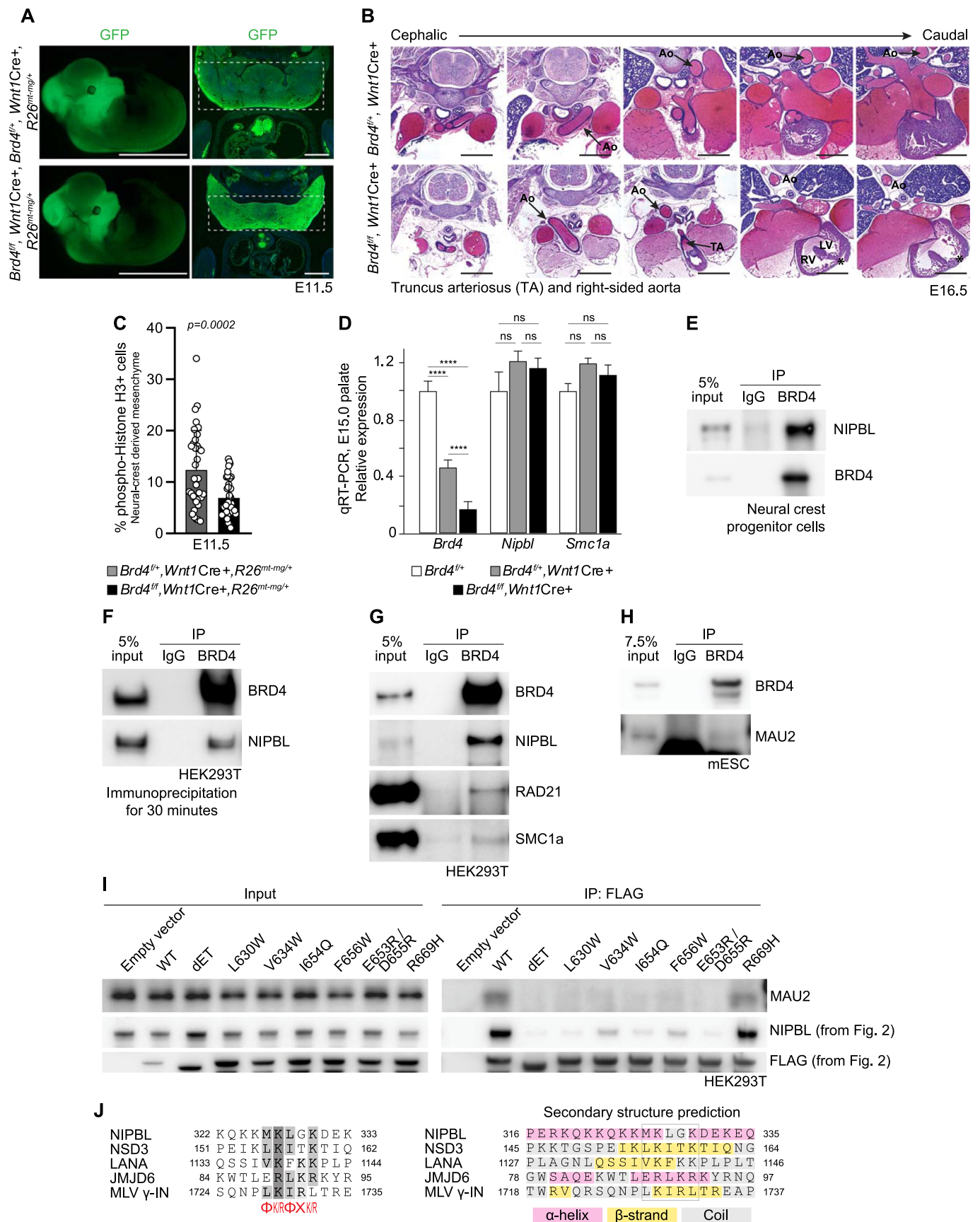
**Extended Data Fig. 1 | See next page for caption.**

**Extended Data Fig. 1 | Characterization of BRD4 in neural crest and the interaction with NIPBL.** (**a**) GFP epifluorescence and immunohistochemistry (coronal section) of E11.5 $Brd4^{f/f}$, $Wnt1$Cre+, $R26^{mt-mg/+}$ and $Brd4^{f/+}$, $Wnt1$Cre+, $R26^{mt-mg/+}$ embryos. Scale bar, epifluorescence: 500 mm; immunohistochemistry: 500 μm. (**b**) Multiple sections of E16.5 $Brd4^{f/f}$, $Wnt1$Cre+ and $Brd4^{f/+}$, $Wnt1$Cre+ embryo showing outflow tract and heart. Mutant demonstrates right-sided aortic arch and truncus arteriosus. (Ao, Aorta; RV, right ventricle; LV, left ventricle; TA, truncus arteriosus). Second image duplicated from Fig. 1. (* denotes sectioning artifact). Scale bar, 1 mm. (**c**) Percentage of phospho-Histone H3 + cells in neural crest-derived craniofacial mesenchyme (each point represents one field of view, 35 ($Brd4^{f/+}$, $Wnt1$Cre+, $R26^{mt-mg/+}$) and 37 ($Brd4^{f/f}$, $Wnt1$Cre+, $R26^{mt-mg/+}$) fields of view total from two embryos, mean and SD shown, student's T-test). (**d**) Expression of indicated genes in E15.0 secondary palate tissue (Unpaired T-test; ****$p < 0.0001$. Error bars denote SEM). Gene expression normalized to the expression of $Hprt1$. (**e**) Immunoprecipitation of endogenous BRD4 blotted for BRD4 and NIPBL (murine neural crest cells, O9-1 cells). (**f**) Immunoprecipitation (30 min) of endogenous BRD4 from and blotted for BRD4 and NIPBL (HEK293T cells)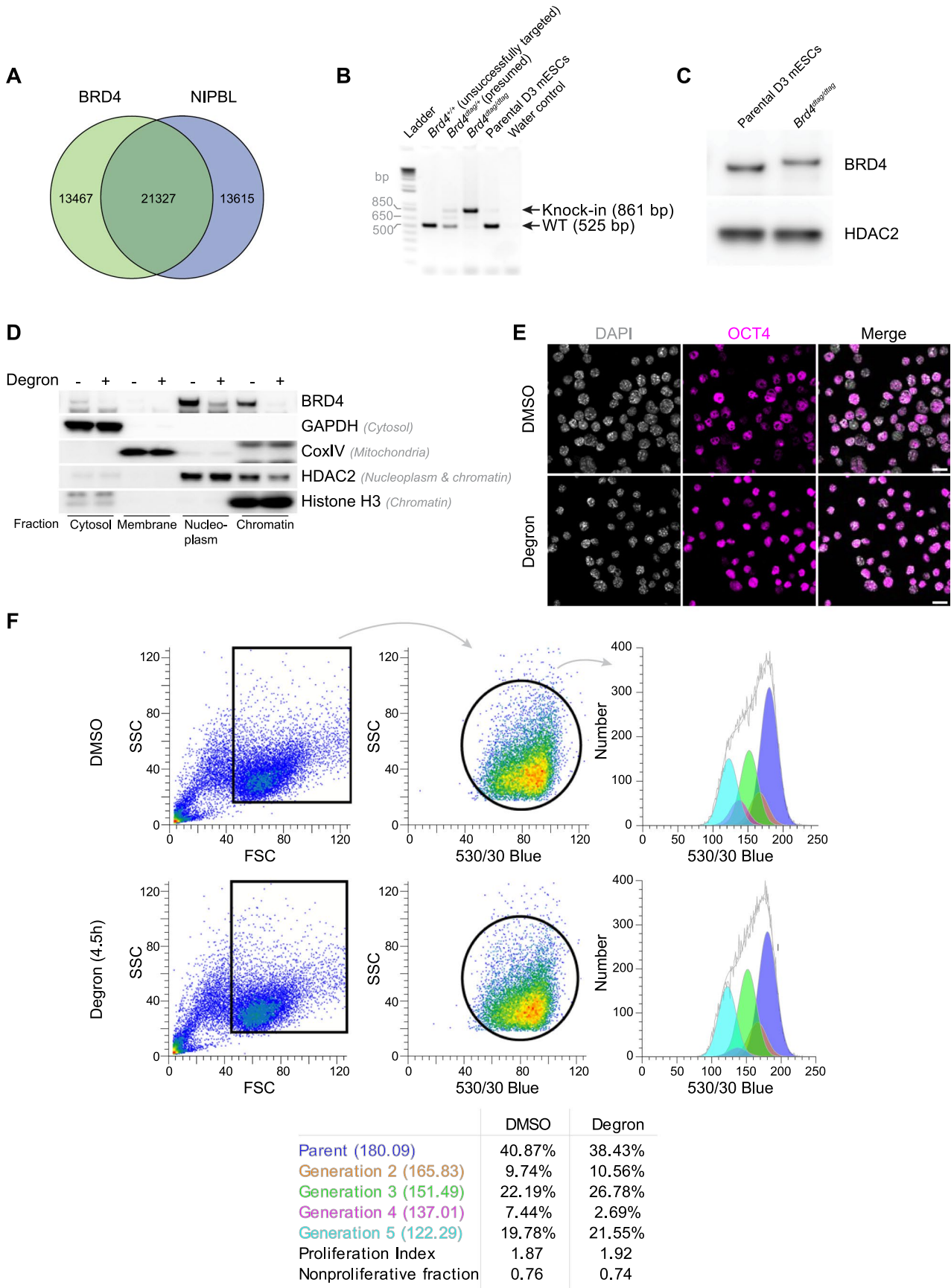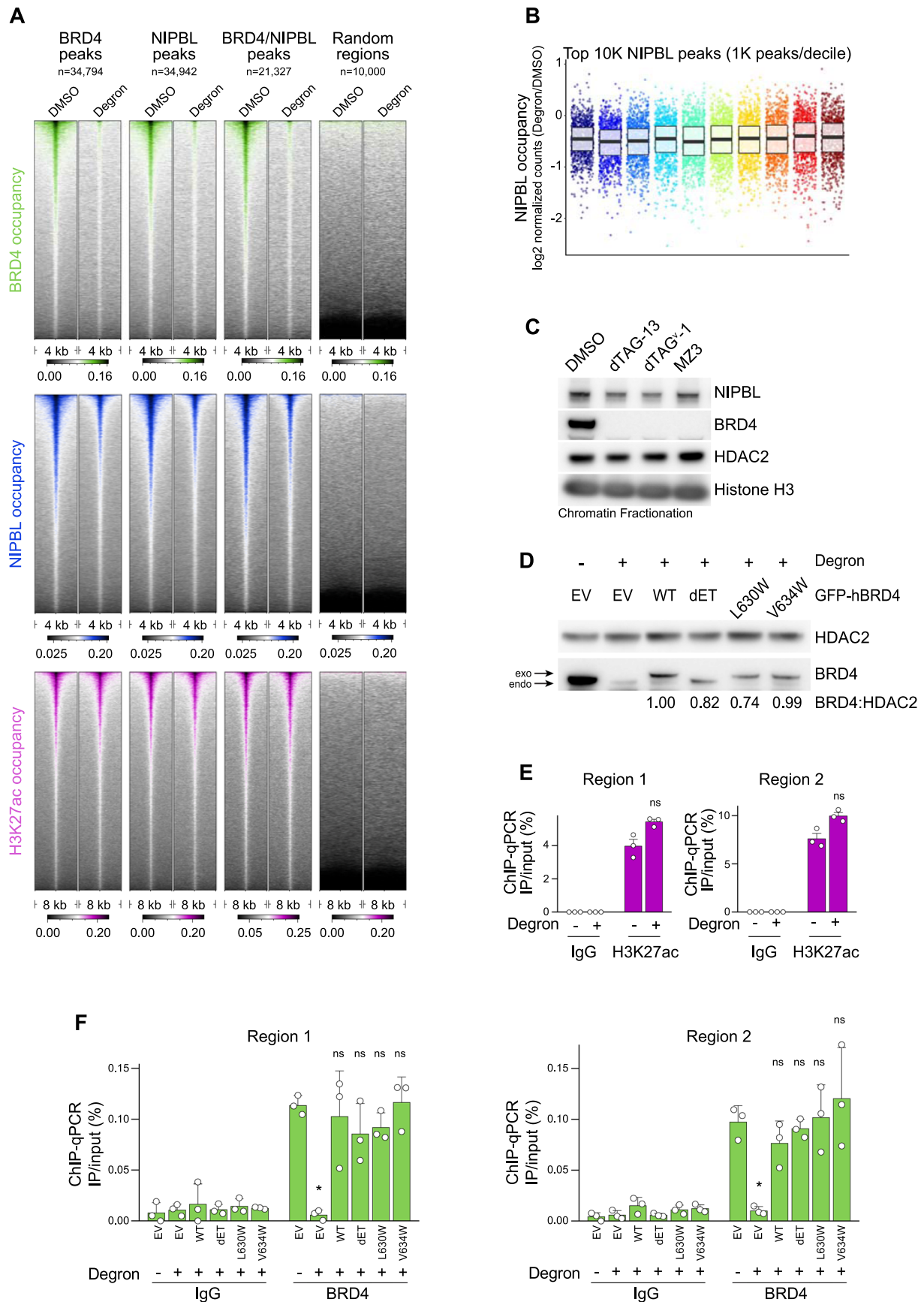. (**g**) Immunoprecipitation of endogenous BRD4 and blotted for indicated proteins (HEK293T cells). (**h**) Immunoprecipitation of endogenous BRD4 and blotted for indicated proteins (mESCs). (**i**) Indicated FLAG-tagged versions of BRD4 immunoprecipitated (HEK293T cells). Immunoblots probed with indicated antibodies. The NIPBL and FLAG immunoblots are reproduced from Fig. 2e as the proteins were all blotted for from the same blot. (**j**) Alignment of BRD4-interacting peptides of NSD3, LANA, JMJD6 and MLV-γ-integrase and putative BRD4-interacting peptide of NIPBL. Residues highlighted by gray are conserved across other peptides. Consensus motif indicated at the bottom (Φ represents a hydrophobic amino acid and X any amino acid). Predicted α-helix, β-strand and coil structures are marked by pink, yellow and gray color, respectively. Predictions based on PSPIRED[71]. The consensus motif is highlighted in the gray box.

**A** BRD4    NIPBL

13467    21327    13615

**B** Ladder / Brd4+/+ (unsuccessfully targeted) / Brd4^dtag/+ (presumed) / Brd4^dtag/dtag mESCs / Parental D3 mESCs / Water control

bp
850 —
650 —
500 —

← Knock-in (861 bp)
← WT (525 bp)

**C** Parental D3 mESCs / Brd4^dtag/dtag

BRD4
HDAC2

**D**

Degron    −  +   −  +   −  +   −  +

BRD4
GAPDH (Cytosol)
CoxIV (Mitochondria)
HDAC2 (Nucleoplasm & chromatin)
Histone H3 (Chromatin)

Fraction    Cytosol    Membrane    Nucleo-plasm    Chromatin

**E** DAPI / OCT4 / Merge

DMSO

Degron

**F**

|  | DMSO | Degron |
|---|---|---|
| Parent (180.09) | 40.87% | 38.43% |
| Generation 2 (165.83) | 9.74% | 10.56% |
| Generation 3 (151.49) | 22.19% | 26.78% |
| Generation 4 (137.01) | 7.44% | 2.69% |
| Generation 5 (122.29) | 19.78% | 21.55% |
| Proliferation Index | 1.87 | 1.92 |
| Nonproliferative fraction | 0.76 | 0.74 |

**Extended Data Fig. 2 | See next page for caption.**

**Extended Data Fig. 2 | Generation of dTAG-BRD4 mouse embryonic stem cell line. (a**) Venn diagram showing the comparison of BRD4 and NIPBL peaks from publicly available datasets (see Methods). (**b**) PCR of genomic DNA from clones of indicated genotype using oligos annealing outside of area of homologous recombination. "Unsuccessfully targeted" is a line which was targeted by sgRNA and Cas9, but dTAG was not inserted. Of clones shown, only *Brd4^dtag/dtag^* was confirmed by Sanger sequencing. (Ladder: Thermo, #10787-018). (**c**) Immunoblot of chromatin fraction from parental and dTAG-BRD4 mESCs. (**d**) Confirmation of fractionation protocol. Cytosol, membrane, nucleoplasm, and chromatin fractions from dTAG-BRD4 mESCs in control and the degron conditions were blotted for indicated proteins. (**e**) OCT4 immunofluorescence from dTAG-BRD4 mESCs in control and the degron conditions. Scale bar, 20 μm. (**f**) Flow cytometry-based analysis of proliferation/doubling time using CellTrace CFSE at 4.5 h post treatment with DMSO or 500 nM dTAG-13. Rectangle and circle in left and middle graphs indicates gate in which cells analyzed using Cell Proliferation tool on ModFIT LT v5.0 (n = 23823 and 23859 cells in DMSO and degron, respectively).

**A**

BRD4 peaks n=34,794 | NIPBL peaks n=34,942 | BRD4/NIPBL peaks n=21,327 | Random regions n=10,000

BRD4 occupancy
NIPBL occupancy
H3K27ac occupancy

**B**

Top 10K NIPBL peaks (1K peaks/decile)

NIPBL occupancy log2 normalized counts (Degron/DMSO)

**C**

NIPBL
BRD4
HDAC2
Histone H3

Chromatin Fractionation

**D**

Degron
GFP-hBRD4
HDAC2
BRD4
BRD4:HDAC2    1.00  0.82  0.74  0.99

exo
endo

**E**

Region 1    Region 2

ChIP-qPCR IP/input (%)

**F**

Region 1    Region 2

ChIP-qPCR IP/input (%)

Extended Data Fig. 3 | See next page for caption.

**Extended Data Fig. 3 | BRD4 regulates NIPBL occupancy.** (**a**) Co-occupancy analysis of BRD4 (green), NIPBL (blue) and H3K27ac (purple) at BRD4, NIPBL, or BRD4/NIPBL peaks as defined in Extended Data Fig. 2a. (**b**) NIPBL occupancy [log2 normalized counts (Degron/DMSO)] across top 10 K peaks. (**c**) Immunoblot of chromatin fractionations from DMSO, dTAG-13 (500 nM), dTAG$^v$-1 (500 nM), and MZ3 (1 μM)-treated cells for 4.5 h for indicated proteins. The samples were derived from the same experiment and blots were processed in parallel. (**d**) Expression of indicated BRD4-mutants in dTAG-BRD4 mESCs upon degradation of endogenous BRD4. HDAC2 is used as a loading control. Relative band intensity ratio (BRD4:HDAC2) is indicated. (**e**) ChIP-qPCR of H3K27ac at regions indicated in Fig. 3e. Two-tailed T-test was used for comparison. Error bars denote the mean + SEM. (**f**) ChIP-qPCR of BRD4 or IgG at the same two regions assayed in Fig. 3f. One-way ANOVA Dunnett's test was used to compare conditions to empty vector transfection with DMSO treatment. *$p < 0.05$. Error bars denote the mean + SD.

**A** Loop comparison

**B** Gained interactions

**C** NIPBL occupancy

**D** Loop stratification

Legend:
- Structural
- Other
- CTCF-Cohesin independent EP loop
- CTCF-Cohesin EP loop

Resistant n=2219
Sensitive n=5298

**E** Change in interaction frequency

RAD21, CTCF, NIPBL, BRD4

**F** Change in interaction frequency (NIPBL peaks)

BRD4 occupancy at NIPBL peaks

NIPBL peak strength: Top decile — Bottom decile

**G** DMSO, mESCs

Jaccard index
Dixon et al. 2012 TADs : DMSO mESCs TADs - 0.82

DMSO, mESCs 1.6e8 bp
Shared 1.95e9 bp
Dixon et al. 2012 2.57e8 bp

**H** Insulation score correlation at TAD boundaries

Spearman correlation = 0.97

**Extended Data Fig. 4 |** See next page for caption.

**Extended Data Fig. 4 | BRD4 maintains higher order chromatin structure.** (**a**) Hi-C matrix comparing c-loop identified loops in DMSO, dTAG-BRD4 mESCs (blue) to mESCs profiled in Mumbach et al., 2016 (black) at two different regions. (**b**) Mean counts/bin of gained interactions in DMSO and the degron conditions. T-test used for comparison. (**c**) NIPBL occupancy at BRD4-sensitive and -resistant loop anchors in DMSO and the degron conditions. (**d**) Stratification of BRD4-resistant and -sensitive loops. Structural loops refer to loops with CTCF and RAD21 peaks at both anchors and 0-1 anchors have H3K27ac peak. CTCF-Cohesin enhancer-promoter (EP) loops refer to loops with H3K27ac, CTCF and RAD21 peaks at both anchors. CTCF-Cohesin independent loops refer to loops with CTCF and RAD21 peaks at 0-1 anchors and both anchors have H3K27ac peak. Other refers to all loops which do not fall into these categories. Anchor regions were extended by 15 kb upstream and downstream for peak intersections. (**e**) Change in interaction frequency at BRD4, NIPBL, RAD21, and CTCF peaks. (**f**) Change in interaction frequency at NIPBL peaks (stratified into deciles of peak strength) upon depletion of BRD4 (left) and BRD4 occupancy (normalized counts) at NIPBL peaks (right) (stratified into deciles of peak strength). (**g**) Hi-C matrix comparing TADs in DMSO, dTAG-BRD4 mESCs (blue) to mESCs profiled in Dixon et al.[51] (black) at two different regions. Adjacent bar plot compares the percentage of basepairs uniquely found in a TAD in DMSO, dTAG-BRD4 mESCs (light blue), Dixon et al.[51] mESCs (black) or shared between the datasets (navy). Jaccard index between datasets 0.82. (**h**) Correlation of insulation score specifically at TAD boundaries between DMSO and the degron conditions.

**A** Compartment analysis
DMSO Degron
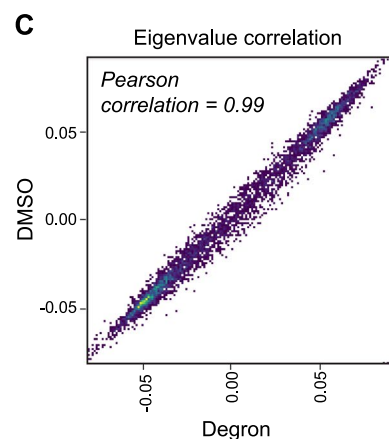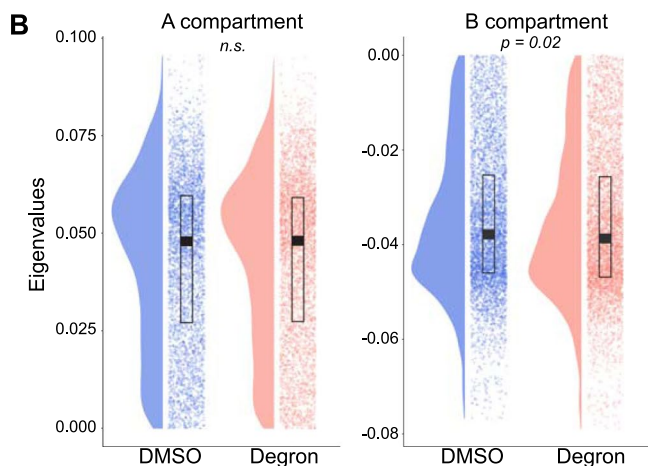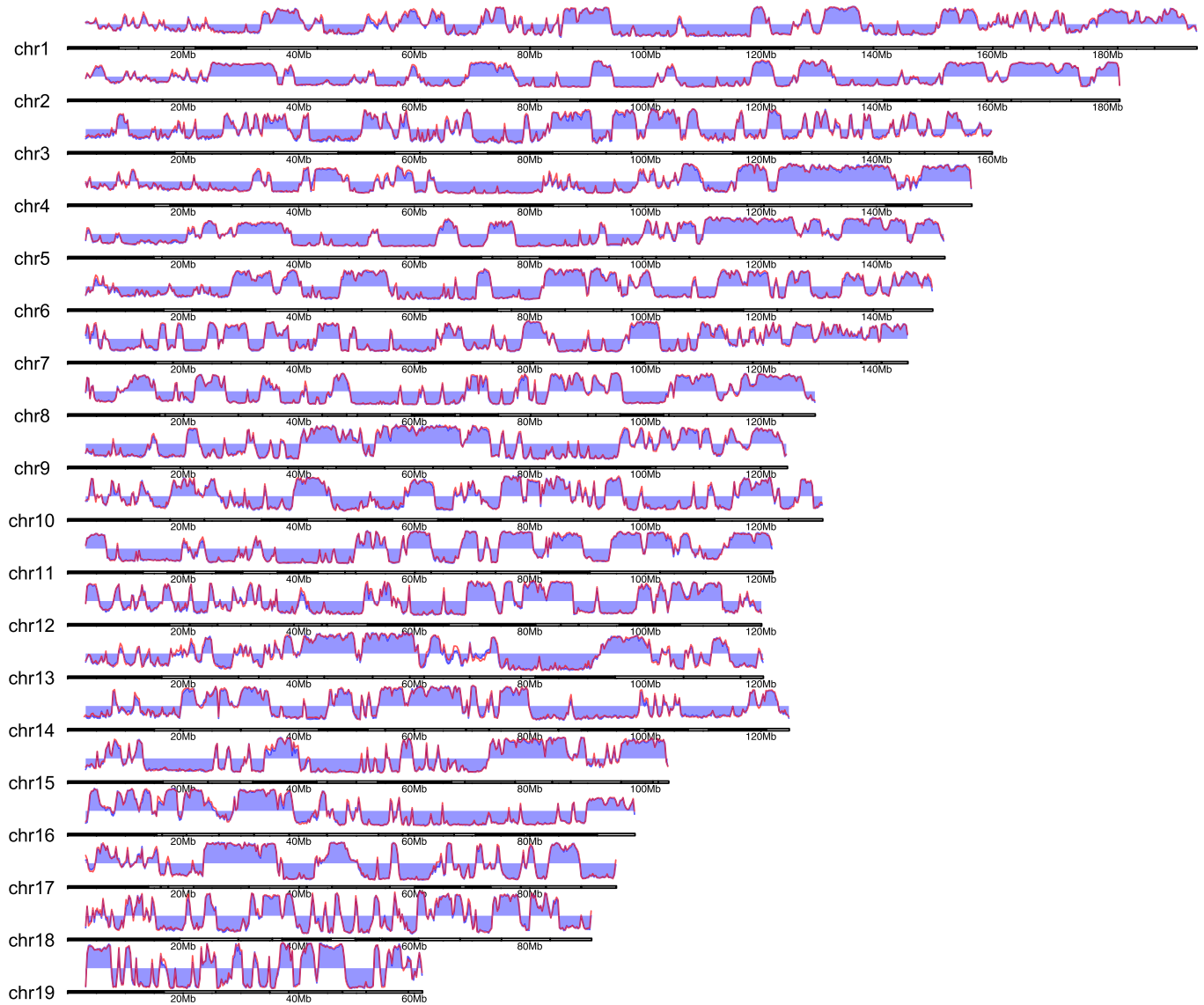


**Extended Data Fig. 5 | BRD4 loss does not affect compartmentalization.** (**a**) Eigenvalues in 250 kb bins across the entire genome in DMSO (blue) and the degron (red) conditions, per chromosome. (**b**) Genome wide comparison of eigenvector values (250 kb bins) in DMSO (blue) and the degron (red) conditions. (**c**) Correlation of eigenvector values between DMSO and the degron conditions. T-test used for comparison.
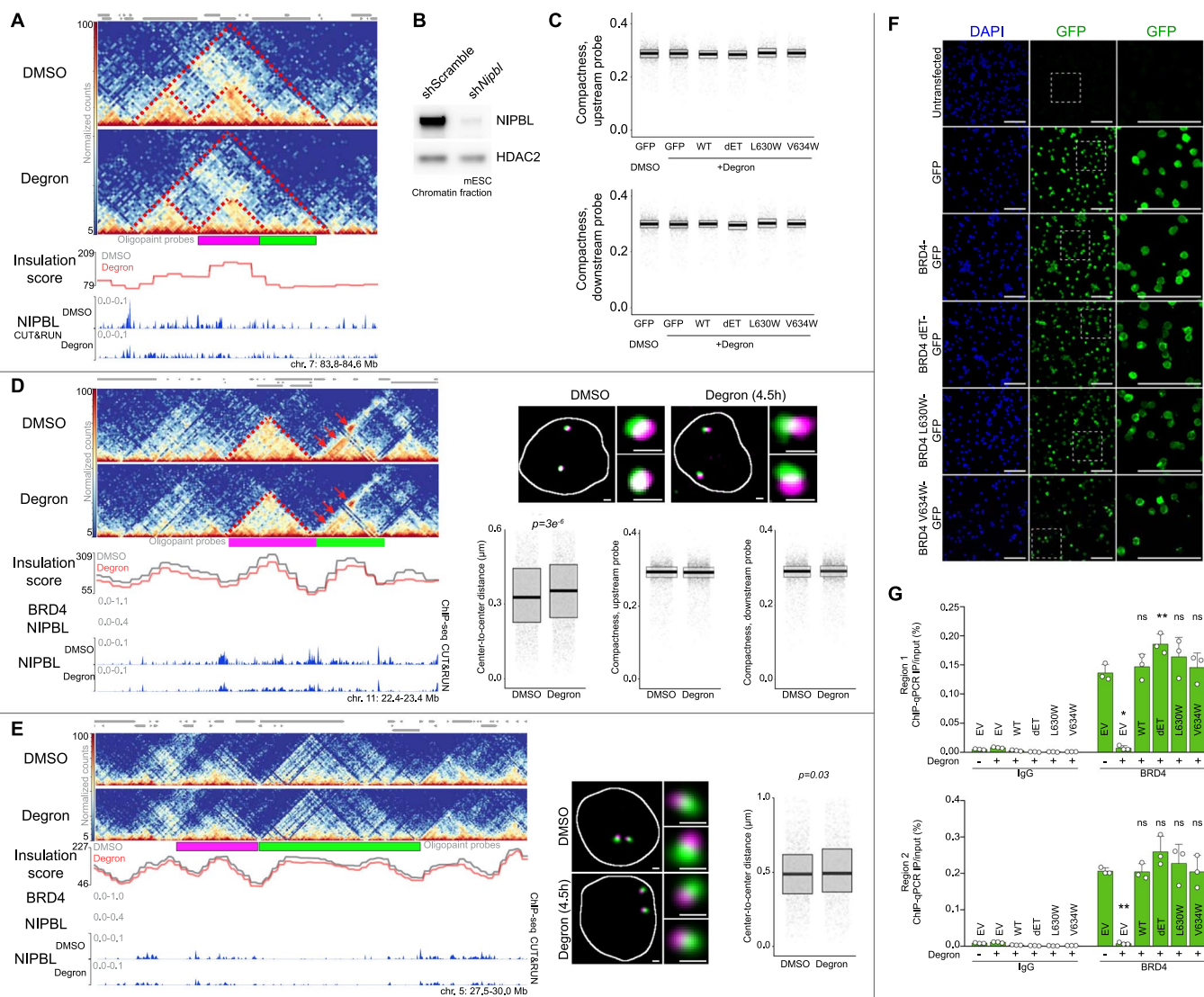
**Extended Data Fig. 6 | Loss of BRD4 abrogates genome folding. (a)** Hi-C matrix (10 kb resolution) of region painted with Oligopaints (as indicated by the green and magenta bars below matrix, from Fig. 5a). Below matrix is insulation score and NIPBL occupancy in DMSO and degron conditions. (**b**) Immunoblot of NIPBL in shScramble and sh*Nipbl* treatment in mESCs. HDAC2 was blotted as a loading control. (**c**) FISH signal compactness (see methods) of upstream and downstream probes used in Fig. 5. (**d**) Hi-C matrix (10 kb resolution) with areas painted with Oligopaints, insulation score, BRD4 and NIPBL occupancy (in wildtype mESCs), NIPBL occupancy in DMSO and degron samples shown below. Area highlighted by red dotted line indicates sub-TAD and arrows point to a domain affected upon BRD4 depletion. On right is a representative image from DMSO and the degron conditions with regions painted indicated below matrix. Below the representative FISH images is the plot of center-to-center signal distances and compactness of FISH signals. For visualization purposes only, only probe center-to-center distances up to 0.6 μm shown. Wilcoxon-rank sum test. Scale bar, 1 μm. (**e**) Hi-C matrix (10 kb resolution) with areas painted with Oligopaints, insulation score, BRD4 and NIPBL occupancy (in wildtype mESCs), and NIPBL occupancy in DMSO and degron samples shown below. In middle is representative image from DMSO and the degron conditions with regions indicated on matrix painted. On right is the plot of center-to-center distances. Wilcoxon-rank sum test used for comparison. Scale bar, 1 μm. All images are maximum-projections. (**f**) Representative GFP immunofluorescence from conditions used in Fig. 5c. Scale bar, 100 μm. (**g**) ChIP-qPCR of BRD4 or IgG at the two regions indicated in Fig. 5a by red bars. One-way ANOVA Dunnett's test was used to compare conditions to empty vector transfection with DMSO treatment. *$p < 0.05$. Error bars denote the mean + SD.
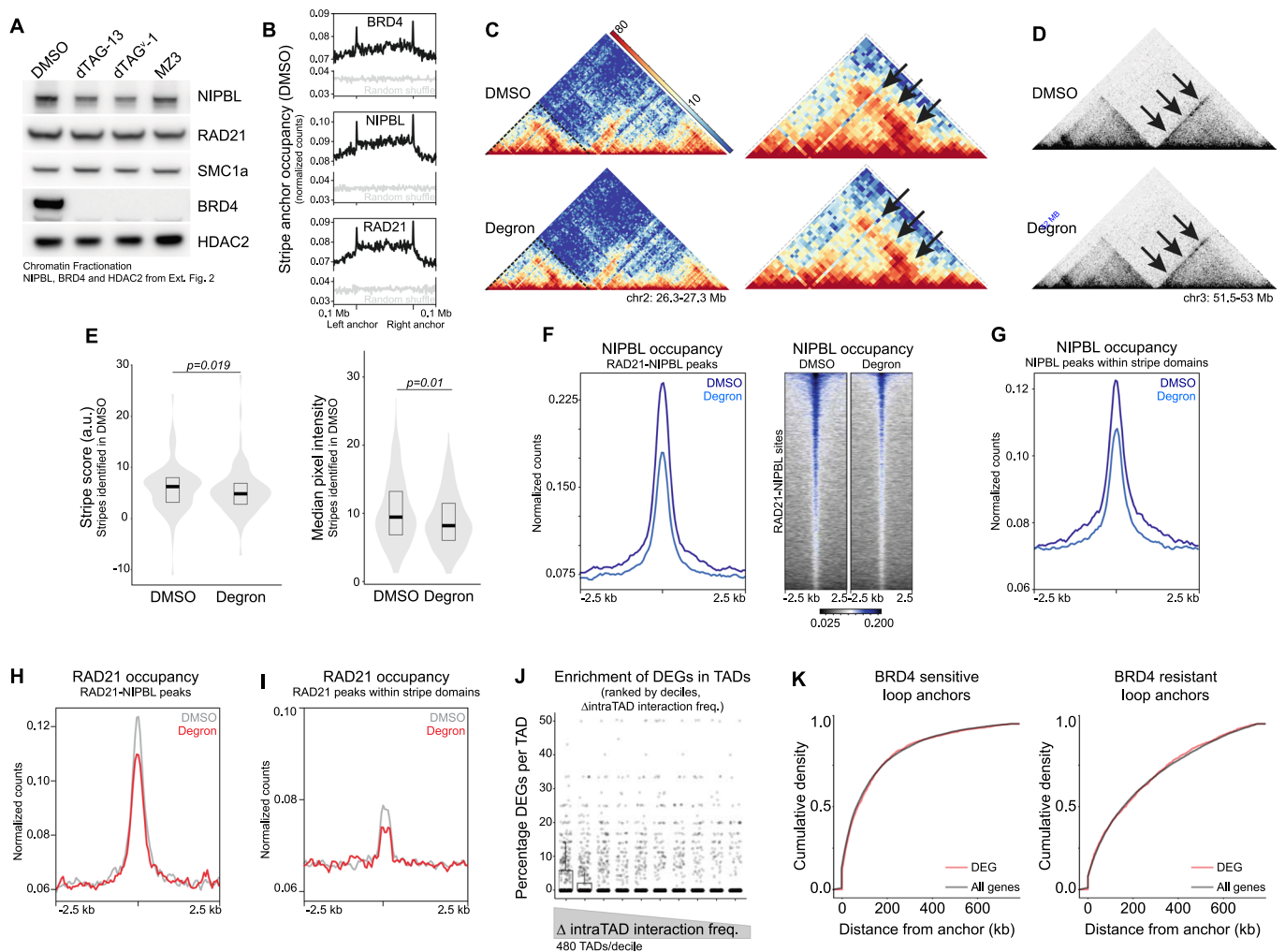
**Extended Data Fig. 7 | BRD4 mediates loop extrusion. (a)** Chromatin fractionation immunoblot of dTAG-BRD4 mESCs treated with DMSO, dTAG-13 (500 nM), dTAG$^v$-1 (500 nM), or MZ3 (1 µM) for 4.5 h. The NIPBL, BRD4 and HDAC2 immunoblots are reproduced from Extended Data Fig. 2f as the proteins were all blotted from the same blot. The samples were derived from the same experiment and blots were processed in parallel. **(b)** Occupancy from public datasets (see methods) of indicated factors (black) and random shuffle (gray) across stripe domains in DMSO-treated dTAG-BRD4 mESCs. Note the enrichment of factor occupancy at stripe anchors. **(c)** Hi-C matrix (top DMSO, bottom Degron) showing an example of a stripe domains (10 kb resolution), which is magnified on the right. Black arrows indicate a stripe domain which is weaker in degron compared to control. Color bar refers normalized count. **(d)** Hi-C matrix (top DMSO, bottom Degron) showing another example of stripe (indicated by arrow) which is weaker in degron compared to DMSO (10 kb resolution). **(e)** Change in stripe score and median intensity of stripe domains in degron compared to DMSO. Stripe domains defined in DMSO condition and same region compared in the degron condition. T-test used for comparison. **(f–i)** Occupancy of NIPBL (F and G) or RAD21 (H and I) at RAD21-NIPBL peaks (F and H) or in stripe domains (G-NIPBL peaks and I-RAD21 peaks) in DMSO and the degron conditions. **(j)** The percentage of differentially expressed genes per TAD is plotted and TADs are broken into descending deciles of change in interaction frequency. Individual data points shown as well as superimposed box and whisker plot (median and interquartile range indicated by box). **(k)** Cumulative density of differentially expressed genes (DEG, FDR < 0.05, |log2FC| > 1, red) or all genes (black) in relation to proximity to BRD4-sensitive (left) and -resistant (right) loop anchors.
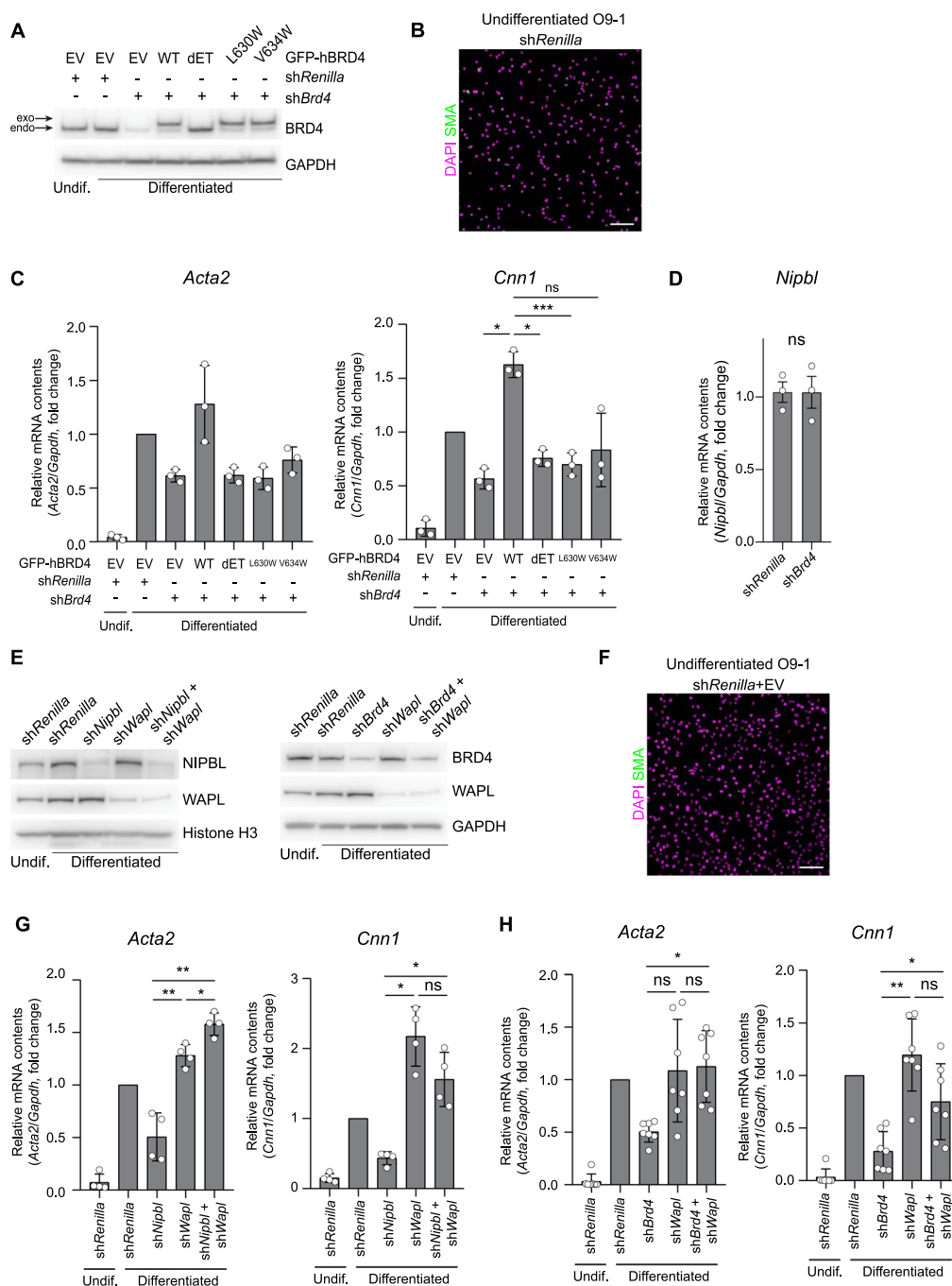
**Extended Data Fig. 8 | BRD4 mediates differentiation of neural crest progenitor cells.** (**a**) Immunoblot showing levels of BRD4 upon depletion of BRD4 and introduction of wildtype BRD4 or various mutants unable to bind NIPBL. EV: empty vector. Undif.: Undifferentiated condition. (**b**) Representative image of undifferentiated O9-1 cells infected with sh*Renilla* and stained with SMA antibody. Scale bar, 100 μm. (**c**) *Acta2* and *Cnn1* expression in indicated conditions. One-way ANOVA Tukey's multiple comparison test is used to compare across conditions (*$p < 0.05$, ***$p < 0.001$). Error bars denote the mean ± SD. Undif.: Undifferentiated condition. (**d**) *Nipbl* expression in *Brd4*-depleted O9-1 cells. Unpaired t-test was used for comparison. All error bars denote the mean ± SEM. (**e**) Immunoblots of BRD4, WAPL and NIPBL in various knockdown conditions. Histone H3 and GAPDH are loading controls. Undif.: Undifferentiated condition. (**f**) Representative image of undifferentiated O9-1 cells infected with sh*Renilla* and transfected with empty vector and stained with SMA antibody. Scale bar, 100 μm. (**g**, **h**) *Acta2* and *Cnn1* expression in indicated conditions. One-way ANOVA Tukey's multiple comparison test is used to compare across conditions (*$p < 0.05$, **$p < 0.01$, ***$p < 0.001$). Error bars denote the mean ± SD. Undif.: Undifferentiated condition.

# nature research

Corresponding author(s): Rajan Jain

Last updated by author(s): 7/16/2021

# Reporting Summary

Nature Research wishes to improve the reproducibility of the work that we publish. This form provides structure for consistency and transparency in reporting. For further information on Nature Research policies, see our Editorial Policies and the Editorial Policy Checklist.

## Statistics

For all statistical analyses, confirm that the following items are present in the figure legend, table legend, main text, or Methods section.

| n/a | Confirmed | |
|---|---|---|
| ☐ | ☒ | The exact sample size ($n$) for each experimental group/condition, given as a discrete number and unit of measurement |
| ☐ | ☒ | A statement on whether measurements were taken from distinct samples or whether the same sample was measured repeatedly |
| ☐ | ☒ | The statistical test(s) used AND whether they are one- or two-sided *Only common tests should be described solely by name; describe more complex techniques in the Methods section.* |
| ☐ | ☒ | A description of all covariates tested |
| ☐ | ☒ | A description of any assumptions or corrections, such as tests of normality and adjustment for multiple comparisons |
| ☐ | ☒ | A full description of the statistical parameters including central tendency (e.g. means) or other basic estimates (e.g. regression coefficient) AND variation (e.g. standard deviation) or associated estimates of uncertainty (e.g. confidence intervals) |
| ☐ | ☒ | For null hypothesis testing, the test statistic (e.g. $F$, $t$, $r$) with confidence intervals, effect sizes, degrees of freedom and $P$ value noted *Give P values as exact values whenever suitable.* |
| ☒ | ☐ | For Bayesian analysis, information on the choice of priors and Markov chain Monte Carlo settings |
| ☒ | ☐ | For hierarchical and complex designs, identification of the appropriate level for tests and full reporting of outcomes |
| ☐ | ☒ | Estimates of effect sizes (e.g. Cohen's $d$, Pearson's $r$), indicating how they were calculated |

*Our web collection on statistics for biologists contains articles on many of the points above.*

## Software and code

Policy information about availability of computer code

| Data collection | Tissue Immunohistochemistry and immunofluorescence images were acquired with Aperio ImageScope v12. Leica Application Suite X v.3 was used for wide-field and confocal image acquisition. Flow data was acquired using the BD FACS Canto II. Immunoblot images were obtained by ImageQuant LAS 500 and LAS 4000. Quantitative RT-PCR and ChIP-qPCR were performed on the ABI 7900HT Fast Real Time PCR system. Sequencing data was obtained using Illumina NextSeq 500/550 platform (CUT&RUN, SLAM-seq) and NovaSeq 6000 (Hi-C). |
|---|---|
| Data analysis | Bowtie2 v1.2.2 : http://bowtie-bio.sourceforge.net/bowtie2/index.shtml<br>fastp v0.20.0: https://github.com/OpenGene/fastp<br>Sambamba v0.7.0: https://lomereiter.github.io/sambamba/<br>DeepTools v3.1.3 : https://deeptools.readthedocs.io/<br>Bedtools v2.29.2: https://bedtools.readthedocs.io/<br>HiC-Pro v2.11.1: https://github.com/nservant/HiC-Pro<br>HiCExplorer v3.6: https://hicexplorer.readthedocs.io/<br>cLoops v0.93: https://github.com/YaqiangCao/cLoops<br>TADtool v0.81: https://github.com/vaquerizaslab/tadtool<br>Coolpuppy v.0.9.5: https://github.com/open2c/coolpuppy<br>Juicer Tools v1.12.03: https://github.com/aidenlab/juicer<br>STAR v2.7: https://github.com/alexdobin/STAR<br>Stripenn v1.1.61: https://github.com/ysora/stripenn<br>Juicebox v1.11.08: https://github.com/theaidenlab/juicebox<br>pyGenomeTracks v3.6: https://github.com/deeptools/pyGenomeTracks<br>Slamdunk v0.4.3  https://github.com/t-neumann/slamdunk<br>ImageJ v1.53c: https://imagej.nih.gov/ij/<br>Prism9: https://www.graphpad.com/scientific-software/prism/<br>R v3.5.2: https://www.r-project.org/ |

OligoMiner: https://github.com/beliveau-lab/OligoMiner
ModFIT LT v5.0: http://www.vsh.com/products/mflt/
DataAssist v3.01: https://www.thermofisher.com/search/results?query=DataAssist
TANGO v0.99: https://github.com/mcib3d/tango/
LI-COR Image Studio v5.2: https://www.licor.com/bio/image-studio-lite/
GeneDoc v2.7.000: https://www.psc.edu/genedoc-user-manual/

For manuscripts utilizing custom algorithms or software that are central to the research but not yet described in published literature, software must be made available to editors and reviewers. We strongly encourage code deposition in a community repository (e.g. GitHub). See the Nature Research guidelines for submitting code & software for further information.

## Data

Policy information about availability of data

 All manuscripts must include a data availability statement. This statement should provide the following information, where applicable:

- Accession codes, unique identifiers, or web links for publicly available datasets
- A list of figures that have associated raw data
- A description of any restrictions on data availability

All raw and processed data generated for this paper is available under accession number GSE169516. Published ChIP-seq datasets used in this study were: BRD4 (GEO: GSM937540); NIPBL (GEO: GSM560350), H3K27ac (GEO: GSM2588454), and RAD21 (GEO: GSM824848). The corresponding processed files for these ChIP-seq datasets, including their peak calls, were obtained from CistromeDB (34084 for BRD4, 2864 for NIPBL, 67169 for H3K27ac, and 39300 for RAD21).Loop calls used for comparison came from published SMC1 HiChIP dataset (Mumbach et al., 2016). Published mESC TAD calls came from Dixon et al, 2012. SLAM-seq, CUT&RUN, and Hi-C analyses were used in this study. No ChIP-seq datasets were generated in this study. See the methods for all relevant details of the pipelines and parameters used.
Mouse genome sequence mm10:  http://ftp.ebi.ac.uk/pub/databases/gencode/Gencode_mouse/release_M10/GRCm38.primary_assembly.genome.fa.gz
Saccharomyces cerevisiae genome sequence sacCer3 : https://hgdownload.soe.ucsc.edu/goldenPath/sacCer3/bigZips/sacCer3.fa.gz
BRD4 ChIP-seq: http://dc2.cistrome.org/api/hgtext/34084/?db=mm10
NIPBL CHIP-seq:  http://dc2.cistrome.org/api/hgtext/2864/?db=mm10
H3K27ac ChIP-seq: http://dc2.cistrome.org/api/hgtext/67169/?db=mm10
RAD21 ChIP-seq: http://dc2.cistrome.org/api/hgtext/39300/?db=mm10

# Field-specific reporting

Please select the one below that is the best fit for your research. If you are not sure, read the appropriate sections before making your selection.

☒ Life sciences        ☐ Behavioural & social sciences        ☐ Ecological, evolutionary & environmental sciences

For a reference copy of the document with all sections, see nature.com/documents/nr-reporting-summary-flat.pdf

# Life sciences study design

All studies must disclose on these points even when the disclosure is negative.

| | |
|---|---|
| Sample size | No statistical test or sample size calculation was performed to pre-determine sample size. For the Oligopaint FISH experiments, a minimum of 500 cells were imaged for each of the at least two replicates, consistent with previous studies (doi: 10.1038/s41588-020-0647-9). The exact number of cells analyzed was dependent on the cell densities in the imaged fields. The sample sizes for our genomics experiments are consistent with previous similar studies in the field (doi: 10.1038/s41588-020-00744-4). The sample size for our differentiation experiments is consistent with our previous differentiation studies (doi: 10.1016/j.stem.2020.12.016, 10.1016/j.cell.2017.09.018, doi: 10.1126/science.aaa6071). |
| Data exclusions | No data were excluded from the analysis. |
| Replication | All experiments in this study were repeated for at least two biological replicates, and data is graphed (representative replicate versus combined replicate data) as indicated. All replicates of each experiment are shown (or yielded identical results if representative replicate shown). All results from technically successfully experiments were analyzed. |
| Randomization | All samples were allocated into groups based on the perturbation (dTAG treatment, shRNA, transfection/infection of BRD4 constructs), and were always accompanied by a corresponding untreated control. |
| Blinding | Analysis of the Oligopaint DNA FISH images was blinded by assigning random, non-descriptive file names and batch processing all image files together. All other data were analyzed simultaneously and computationally using identical pipelines, therefore blinding was not relevant. No manual scoring was used in this study. |

# Reporting for specific materials, systems and methods

We require information from authors about some types of materials, experimental systems and methods used in many studies. Here, indicate whether each material, system or method listed is relevant to your study. If you are not sure if a list item applies to your research, read the appropriate section before selecting a response.

## Materials & experimental systems

| n/a | Involved in the study |
|-----|----------------------|
| ☐ | ☒ Antibodies |
| ☐ | ☒ Eukaryotic cell lines |
| ☒ | ☐ Palaeontology and archaeology |
| ☐ | ☒ Animals and other organisms |
| ☒ | ☐ Human research participants |
| ☒ | ☐ Clinical data |
| ☒ | ☐ Dual use research of concern |

## Methods

| n/a | Involved in the study |
|-----|----------------------|
| ☒ | ☐ ChIP-seq |
| ☐ | ☒ Flow cytometry |
| ☒ | ☐ MRI-based neuroimaging |

## Antibodies

| | |
|---|---|
| Antibodies used | Immunohistochemistry and Immunofluorescence was performed using the following primary antibodies: Goat polyclonal anti-GFP (1:100, Abcam #ab6673), Rabbit polyclonal anti-GFP (1:100, Abcam #ab290), Rabbit polyclonal anti-BRD4 (1:2000, Bethyl #A301-985A100 Lot#7), Rabbit polyclonal anti-phospho-histone H3 (Ser10) (1:20, Cell signaling #9701L Lot#17), Mouse monoclonal anti-SMA clone 1A4 (1:200, Sigma #A5228 Lot#065M4762V), anti-OCT4 (1:200, Abcam #ab19857 Lot#GR3173193-1) and Cy3 conjugated SMA antibody (1:5000, Sigma #C6198)<br><br>Secondary antibodies used were: Alexa fluor 555 donkey anti-rabbit IgG(H+L) (1:250, Invitrogen #A31572 Lot#2088692), Alexa fluor 488 donkey anti-goat IgG(H+L) (1:250, Invitrogen #A11055), Alexa Fluor Plus 488 (1:1000, Thermo Fisher #A32731) and Goat anti-Mouse IgG Secondary Antibody, Alexa Fluor Plus 488 (1:1000, Thermo Fisher #A10680 Lot#2064014) and 555 (1:1000, Thermo Fisher #A32727 Lot#UL287768)]<br><br>Immunoprecipitation was performed using: rabbit IgG (2 μg, Cell Signaling #2729 Lot#9), anti-BRD4 (2 μg, Bethyl #A301-985A100 Lot#7), anti-NIPBL (2 μg, Bethyl #A301-779A Lot#4), anti-FLAG (2 μg, Sigma #F1804 Lot#SLCD3524) or anti-GFP (2 μg, Abcam #290). Chromatin immunoprecipitation was performed using: rabbit Polyclonal Anti-NIPBL [2μg, Bethyl Laboratories #A301-779A Lot#4], rabbit polyclonal H3K27ac (2μg, Abcam #ab4729 Lot#GR3252404-1) and normal rabbit IgG (2 μg, Cell signaling #2729S Lot#9).<br>Immunoblotting was performed with the following primary antibodies: anti-BRD4 (1:2000, Bethyl #A301-985A100 Lot#7), anti-NIPBL (1:2000, Bethyl #A301-779A Lot#4), anti-FLAG (1:2000, Sigma #F1804 Lot#SLCD3524), anti-GFP (1:2000, Abcam #290), anti-NSD3 (1:1000, Cell signaling #92056 Lot#1), anti-Histone H3 (1:10000, Abcam #1791 LotGR3308902), anti-acetylated Histone H4 (1:1000, Santa cruz #sc-377520), anti-MAU2 (1:1000; Thermo Fisher #24770-1-AP), anti-WAPL (1:1000, Cell signaling #77428 Lot#1), anti-SMC1a (1:1000, Invitrogen # PA5-29122 Lot#TD2558933D) and anti-RAD21 (1:1000, Abcam #992 Lot#GR3310168-7), anti-HDAC2 (1:1000, Cell signaling #5113 Lot#1), anti-GAPDH (1:1000, Cell signaling #2118 Lot#14), and anti-CoxIV (1:1000, Cell signaling #11967 Lot#3). Secondary antibodies used were: anti-rabbit IgG, HRP-linked antibody (1:5000, Cell signaling #7074 Lot#29) and anti-mouse IgG, HRP-linked antibody (1:10000, Cell signaling #7076 Lot#34) |
| Validation | All commercial antibodies were validated according to the manufacturer and that data can be found on the manufacturer website for each antibody (see below also). All antibodies except for GFP and FLAG were validated to recognize human and mouse antigens according to the manufacturer. All antibodies produced a band of expected size by immunoblot and cellular localization by immunofluorescence as expected. BRD4, NIPBL, NSD3, SMC1a, RAD21 and WAPL antibodies were further validated by the absence of band following depletion of each protein by dTAG or shRNA treatment. FLAG and GFP antibodies were validated with non-transfected samples by immunoblotting and immunofluorescence.<br><br>Validation statements are also available from manufacturer's website:<br>Goat polyclonal anti-GFP (Abcam #ab6673): https://www.abcam.com/gfp-antibody-ab6673.html<br>Rabbit polyclonal anti-GFP (Abcam #ab290): https://www.abcam.com/gfp-antibody-ab290.html<br>Rabbit polyclonal anti-BRD4 (Bethyl #A301-985A100 Lot#7): https://www.bethyl.com/product/A301-985A100/BRD4+Antibody<br>Rabbit polyclonal anti-phospho-histone H3 (Ser10) (Cell signaling #9701L Lot#17): https://www.cellsignal.com/products/primary-antibodies/phospho-histone-h3-ser10-antibody/9701<br>Mouse monoclonal anti-SMA clone 1A4 (Sigma #A5228 Lot#065M4762V): https://www.sigmaaldrich.com/US/en/product/sigma/a5228<br>Rabbit polyclonal anti-OCT4 (Abcam #ab19857 Lot#GR3173193-1): https://www.abcam.com/oct4-antibody-ab19857.html<br>Mouse monoclonal Cy3-conjugated SMA antibody (sigma #C6198): https://www.sigmaaldrich.com/US/en/product/sigma/c6198?context=product<br>Mouse monoclonal anti-FLAG clone M2 (Sigma #F1804 Lot#SLCD3524): https://www.sigmaaldrich.com/US/en/product/sigma/f1804<br>Rabbit polyclonal H3K27ac (Abcam #ab4729 Lot#GR3252404-1): https://www.abcam.com/histone-h3-acetyl-k27-antibody-chip-grade-ab4729.html<br>Rabbit monoclonal anti-NSD3 (Cell signaling #92056 Lot#1): https://www.cellsignal.com/products/primary-antibodies/whsc1l1-d4n9n-rabbit-mab/92056<br>Rabbit polyclonal anti-Histone H3 (Abcam #1791 LotGR3308902): https://www.abcam.com/histone-h3-antibody-nuclear-marker-and-chip-grade-ab1791.html<br>Mouse monoclonal anti-acetylated Histone H4 (Santa cruz #sc-377520): https://www.scbt.com/ko/p/ac-histone-h4-antibody-e-5<br>Rabbit polyclonal anti-MAU2 (Thermo Fisher #24770-1-AP): https://www.thermofisher.com/antibody/product/SCC4-Antibody-Polyclonal/24770-1-AP<br>Rabbit monoclonal anti-WAPL (Cell signaling #77428 Lot#1): https://www.cellsignal.com/products/primary-antibodies/wapl-d9j1u-rabbit-mab/77428<br>Rabbit polyclonal anti-SMC1a (Invitrogen # PA5-29122 Lot#TD2558933D): https://www.thermofisher.com/antibody/product/SMC1-Antibody-Polyclonal/PA5-29122<br>Rabbit polyclonal anti-RAD21 (Abcam #992 Lot#GR3310168-7): https://www.abcam.com/rad21-antibody-ab992.html<br>Mouse monoclonal anti-HDAC2 (Cell signaling #5113 Lot#1): https://www.cellsignal.com/products/primary-antibodies/hdac2-3f3-mouse-mab/5113 |

Rabbit monoclonal anti-GAPDH (Cell signaling #2118 Lot#14): https://www.cellsignal.com/products/primary-antibodies/gapdh-14c10-rabbit-mab/2118
Mouse monoclonal anti-CoxIV (Cell signaling #11967 Lot#3): https://www.cellsignal.com/products/primary-antibodies/cox-iv-4d11-b3-e8-mouse-mab/11967
Alexa fluor 555 donkey anti-rabbit IgG(H+L) (Invitrogen #A31572 Lot#2088692): https://www.thermofisher.com/antibody/product/Donkey-anti-Rabbit-IgG-H-L-Highly-Cross-Adsorbed-Secondary-Antibody-Polyclonal/A-31572
Alexa fluor 488 donkey anti-goat IgG(H+L) (Invitrogen #A11055): https://www.thermofisher.com/antibody/product/Donkey-anti-Goat-IgG-H-L-Cross-Adsorbed-Secondary-Antibody-Polyclonal/A-11055
Alexa Fluor Plus 488 (Thermo Fisher #A32731): https://www.thermofisher.com/antibody/product/Goat-anti-Rabbit-IgG-H-L-Highly-Cross-Adsorbed-Secondary-Antibody-Polyclonal/A32731
Alexa Fluor Plus 488 Goat anti-Mouse IgG (Thermo Fisher #A10680 Lot#2064014): https://www.thermofisher.com/antibody/product/Goat-anti-Mouse-IgG-IgM-H-L-Secondary-Antibody-Polyclonal/A-10680
Alexa Fluor Plus 555 Goat anti-Mouse IgG  (Thermo Fisher #A32727 Lot#UL287768): https://www.thermofisher.com/antibody/product/Goat-anti-Mouse-IgG-H-L-Highly-Cross-Adsorbed-Secondary-Antibody-Polyclonal/A32727

# Eukaryotic cell lines

Policy information about cell lines

| | |
|---|---|
| Cell line source(s) | HEK293T and mES cells were purchased from ATCC (#CRL-11268 and  #CRL-1934 respectively). O9-1 neural crest cell line was purchased from Sigma (#SCC049). dTAG-BRD4 mES cells were generated by CRISPR as indicated in methods. |
| Authentication | Cell lines were authenticated by assessing cell morphology, the expression of key marker genes by RT-qPCR, immunoblotting, and immunofluorescence, and susceptibility to antibiotics where applicable. |
| Mycoplasma contamination | Cells were regularly tested using LookOut Mycoplasma PCR Detection Kit (Sigma, #MP0035) and confirmed free of mycoplasma. |
| Commonly misidentified lines (See ICLAC register) | No commonly misidentified lines were used. |

# Animals and other organisms

Policy information about studies involving animals; ARRIVE guidelines recommended for reporting animal research

| | |
|---|---|
| Laboratory animals | Brd4 floxed mice were obtained from Keiko Ozato's laboratory (Lee et al., 2017), and Wnt1Cre mice were obtained from Jackson laboratories (#022137). R26mt-mg mice were obtained from Jackson Laboratories (Muzumdar et al., 2007). Mice were maintained on mixed CD1/B6/129 genetic backgrounds. Littermate embryos were analyzed in all experiments unless otherwise noted. Since only embryos were analyzed in this study, the sex of the embryo was not determined. The age of embryos analyzed is indicated in the relevant figure (legend). Animals were housed in a facility set to 72 degrees (range: 68-76 degrees) and humidity ranged from 30-70%, depending on the time of year. Mice were housed in an AAALAC-accredited facility under a 12:12-h light:dark cycle in same-sex groups of no more than 5 animals per cage in static polycarbonate microisolation cages (Max 75, Alternative Design, Siloam Springs, AR) containing disposable bedding (0.12-in. Bed-O-Cobs, The Andersons, Maumee, OH) with cotton squares (Ancare, Bellmore, NY) for environmental enrichment. Mice were fed standard pelleted laboratory rodent chow (no. 5001, LabDiet, St Louis, MO) without restriction and received municipal water supplied by bottle. Sentinel mice in the facility were tested routinely and were found to be free from fur mites, pinworms, and contagious pathogens, including mouse hepatitis virus, mouse parvoviruses, rotavirus, ectromelia virus, Sendai virus, pneumonia virus of mice, Theiler murine encephalomyelitis virus, reovirus, Mycoplasma pulmonis, lymphocytic choriomeningitis virus, mouse adenovirus, and polyomavirus. Procedures were approved by the University of Pennsylvania's IACUC. |
| Wild animals | This study did not include wild animals. |
| Field-collected samples | This study did not include field-collected animals. |
| Ethics oversight | All animal experiments were performed in accordance with protocols approved by the University of Pennsylvania Institutional Animal Care and Use Committee. |

Note that full information on the approval of the study protocol must also be provided in the manuscript.

# Flow Cytometry

## Plots

Confirm that:

☒ The axis labels state the marker and fluorochrome used (e.g. CD4-FITC).

☒ The axis scales are clearly visible. Include numbers along axes only for bottom left plot of group (a 'group' is an analysis of identical markers).

☒ All plots are contour plots with outliers or pseudocolor plots.

☒ A numerical value for number of cells or percentage (with statistics) is provided.

## Methodology

**Sample preparation**

Estimation of mESC proliferation via CellTrace CFSE (ThermoFisher #C34554) labelling was carried out per manufacturers' instructions with modifications. Briefly, mESCs were seeded on 0.1% bovine gelatin (Sigma #G9391-500g) coated 24-well plates approximately two days prior in order to attain an optimum confluency of approximately 80%. Two extra wells were seeded to serve as unlabeled controls. Any proliferation effects from acute BRD4 degradation were assessed via a time course extending over 4.5 hours. 18 hours prior to treatment with DMSO or 500 nM of dTAG-13, growth medium was removed (except for unstained controls), and gently washed twice with pre-warmed 1x PBS to remove all growth medium. Stock CellTrace CFSE was diluted in pre-warmed 1x PBS (loading solution) to a final concentration of 1 μM/well and added to each well. To ensure efficient labelling, cells were incubated with the loading solution at 37°C for 20 minutes in the dark. Following incubation, the loading solution was aspirated, and cells were washed twice with mESC growth medium. Fresh mESC medium was added to all wells and cells were incubated until initiation of dTAG treatment. The following day, growth medium was removed and replaced with pre-warmed medium containing 500 nM of dTAG-13 or DMSO for 4.5 hours. Cells were then harvested via gentle agitation after incubation with Accutase (Sigma #A6964) for 5 minutes and collected via centrifugation at 2500 rpm for 3 minutes at 4°C. Cell pellets were washed twice and resuspended in 1x PBS to ensure a single cell suspension. The cell suspension was diluted 1/10 in 1x PBS containing 1% FCS, transferred into separately labelled flow tubes and briefly vortexed prior to loading onto the flow cytometer. Flow data was acquired using a low flow rate on the BD FACS Canto II machine (BD Biosciences, USA) with a 488 nm excitation and a 530/30-nm bandpass emission filter. Proliferation analysis and generational assessment was carried out using the Cell Proliferation tool on the ModFIT LT v5.0 software (Verity Software House, http://www.vsh.com/products/mflt/).

**Instrument**

BD FACS Canto II machine (BD Biosciences, USA)

**Software**

ModFit LT 5.0

**Cell population abundance**

No cell sorting method was employed. The viability of the cell population was estimated at around ~95%.

**Gating strategy**

Debris was removed by gating on the main cell population using the FSC/SSC gating strategy. The CellTrace CFSE positive population was thresholded based on an unstained mock DMSO treated sample. Identical gates were applied to all conditions.

☒ Tick this box to confirm that a figure exemplifying the gating strategy is provided in the Supplementary Information.